Thermodynamics of Reaction between Gas-Turbine Ceramic Coatings and Ingested CMAS Corrodents

Gustavo Costa^{1*}, Bryan J. Harder¹, Valerie L. Wiesner¹, Dongming Zhu¹, Narottam Bansal¹, Kang N. Lee¹, Nathan S. Jacobson¹, Denys Kapush², Sergey V. Ushakov², Alexandra Navrotsky²

¹NASA Glenn Research Center, 21000 Brookpark Road, Cleveland, OH, 44135, USA ²Peter A. Rock Thermochemistry Laboratory and NEAT ORU, University of California Davis, Davis, CA 95616, USA

The thermodynamic stability of ceramic coatings with respect to their reaction products is crucial to develop more durable coating materials for gas-turbine engines. Here, we report direct measurements using high temperature solution calorimetry of the enthalpies of reaction between some relevant ceramic coatings and a corrosive molten silicate. We also report the enthalpy of mixing between the coatings and molten silicate after combining the results measured by high temperature solution calorimetry with enthalpies of fusion measured by drop-and-catch (DnC) calorimetry and differential thermal analysis (DTA). The enthalpies of solution of selected silicate and zirconia based coatings and apatite reaction products are moderately positive except for 7YSZ. Apatite formation is only favorable over coating dissolution in terms of enthalpy for 7YSZ. The enthalpies of mixing between the coatings and the molten silicate are less exothermic for Yb₂Si₂O₇ and CaYb₄Si₃O₁₃ than for 7YSZ, indicating lower energetic stability of the latter against molten silicate corrosion. The thermochemical results explain and support the very corrosive nature of CMAS melts in contact with ceramic coatings.

Introduction

In order to meet an ever increasing demand for improved fuel efficiencies, gas turbines are constantly challenged to operate at more elevated temperatures with reduced cooling requirements. While these conditions decrease fuel consumption and greenhouse emissions, a new set of design challenges need to be met for durable engine performance. For advanced gas turbine components, the exposure of mineral dust particles at high temperatures is the major longstanding durability challenge. 1 These aerosol particles enter the hot combustion stream of a gas-turbine engine and stick to hot surfaces. The silicate deposits[†] then melt on the protective coatings at high temperatures, resulting in premature failure.² In aircraft turbines, particulate ingestion occurs during and after take-off since the aerosols can reach altitudes up to 12 km.3 As shown in the example in Fig. 1, some of the aerosol particles passing through the engine collide with internal surfaces, deposit, and melt leading to corrosion. Although other deleterious processes occur due to this exposure (e.g. erosion or glass infiltration through cracks and channels), our discussion is focused on the thermochemical interaction between molten deposits and the coatings. The particle size, shape, velocity and melting temperature dictate the deposition rate on the surfaces.⁴ A significant deposition can occur even when only a small mass fraction (few percent or less) of particles of the total material delivered to the surface melts.⁴ Failure of the engine components by corrosion, erosion, clogging of the cooling holes can result in catastrophic losses such as those of the GE CF6-80C2 engines during a Boeing 747-400 flameout after entering an ash cloud expelled from the Mt. Redoubt volcano near Anchorage, AK. The chemically induced damage of the ceramic coating depends on its composition and structure and

-

[†]For a given silicate composition first liquid may form \sim above 1223 K or eutectic reaction may take place \sim above 1458 K when particles deposit on the coating.

on the chemical composition and concentration of the aerosol, which vary according to the source regions (e.g. arid regions such as deserts, semi-deserts, and areas of recent volcanic activity). 6,7 The mineral dust aerosols have compositions mainly in the CaO-MgO-Al₂O₃-SiO₂ system (CMAS)². In many turbine components, coatings are used to protect the underlying material from thermal or environmental effects.^{2,8} Thermal barrier coatings, or TBCs, are typically used on a metallic substrate (typically a Ni-based superalloy) with a metallic bond coat. The TBC functions to reduce heat flux and the most common material used is 4YSZ or ZrO₂-4Y₂O₃ (YSZ, yttria-stabilized zirconia; rare-earth content in this manuscript is given mol percent although 7YSZ in weight percent is more commonly used in the literature). TBCs made from 4YSZ are a mature technology and in use on aircraft today. 8-12 In contrast, environmental barrier coatings, or EBCs, are intended to act as a barrier to chemically corrosive agents, particularly water vapor in the case of silicon-based ceramics such as silicon carbide (SiC). 13-15 EBCs are currently being used on SiC/SiC ceramic matrix composites (CMCs). EBCs were first applied on CMC shrouds of the LEAP engine manufactured by GE and Safran in 2016¹⁶ and are still a maturing technology. EBCs and TBCs are both susceptible to attack by CMAS corrosion, and therefore the various melt properties, mechanisms of CMAS-coating reactions, and strategies to mitigate coating degradation have been investigated extensively.^{2, 17-34} One of the strategies of mitigating CMAS melt penetration in protective coatings is to promote formation of reaction crystalline products to retard molten CMAS infiltration. A crystalline phase known as apatite has been identified as a potential reaction product for CMAS glasses. Formation of apatite can retard CMAS penetration by fast precipitation of a Ca-containing phase which can block further infiltration while also destabilizing the melt via removal of calcium leading to its crystallization above the melting point of the initial melt composition.^{2, 17-34}.

Although the interaction between CMAS and ceramic coatings has been studied for 21 years¹, the majority of experiments still rely on the analysis of post annealed (furnace and burner rig tests) CMAS powder applied on ceramic coating substrates.² Recently, several strategies based on qualitative approaches have been explored to mitigate coating degradation. One seeks to design coatings that are thermodynamically stable relative to their reaction products.² A second, e.g. apatite formation described above, involves the idea of maximizing the reaction between the coating and CMAS to produce other crystalline phases that are relatively stable in contact with the melt and thus minimize its penetration depth.^{2,17-34} A third strategy involves the concept of a sacrificial ceramic layer to neutralize the melt before it reaches the underlayers and other structural components.² While all these approaches may have merit, there are still only limited thermodynamic data to quantify the energetics of phase equilibria of molten CMAS and ceramic coatings. To date, a number of very useful computed thermodynamic phase diagrams relevant to CMAS induced corrosion have been developed from detailed phase studies. However, quantitative thermodynamics is still needed to further refine these databases and add to our understanding.

In this study we have used high temperature solution calorimetry³⁵⁻⁴¹ (HT solution calorimetry) at 1723 K to directly measure the enthalpies of reaction between some selected ceramic coatings and molten CMAS. This technique was complemented in selected samples with drop-and-catch (DnC) calorimetry⁴² and differential thermal analysis (DTA) above 1773 K^{43, 44} to measure the enthalpy of fusion required for the calculation of their enthalpy of mixing with molten CMAS. We have selected the TBC compositions 7YSZ, 31YSZ and 16RESZ; EBC compositions Y₂Si₂O₇ and Yb₂Si₂O₇; and the apatites CaY₄Si₃O₁₃ and CaYb₄Si₃O₁₃ for the HT solution calorimetric measurements. 7YSZ was selected for DnC calorimetry, and Yb₂Si₂O₇ and

 $CaYb_4Si_3O_{13}$ were selected for DTA since their melting points fall into the temperature range of the instrument. The selected TBC coating compositions are current being evaluated for use and the EBCs are current state-of-the art.¹⁵ The yttrium and ytterbium apatites ($CaY_4Si_3O_{13}$ and $CaYb_4Si_3O_{13}$) were selected as they are well-documented corrosion products between TBCs or EBCs and CMAS.^{2,17-34}

Experimental Materials and Methods

1 - Sample preparation and characterization

1.1 - TBC preparation procedure and characterization

The zirconia based coatings were prepared by air plasma spray (APS) deposition. Details of sample preparation, chemical and structural characterization is given in our previous work.¹⁸

1.2 - EBC preparation procedure

Yttrium disilicate (99.9%, Praxair) and ytterbium disilicate (99.9%, Praxair) powder samples were heat treated in air to 1773 K at 10 K/min with a 10 h hold. The heat treatment was performed to promote coarsening of small particles and/or crystallization of amorphous material that might be present in the as-purchased disilicate powders.

1.2.1 – EBC chemical composition

The chemical composition of yttrium and ytterbium disilicates was measured by energy dispersive X-ray spectroscopy (EDS) using an X-Max^N energy-dispersive X-ray silicon drift detector (EDS-SSD) (Oxford Instruments, Abingdon, United Kingdom) mounted in a Tescan MAIA3 TriglavTM scanning electron microscope (Brno – Kohoutovice, Czech Republic). At least three different grains of each sample were probed by EDS spot analysis.

1.2.2 - EBC X-ray diffraction

XRD data of the heat treated yttrium and ytterbium disilicates powder samples were acquired from 10° to 120 ° 2θ with a step size of 0.020° and a collection time of 0.25 s·step⁻¹ on a D8 Discover diffractometer (Bruker-AXS GmbH, Karlsruhe, Germany). The samples were rotated at 30 rpm. Crystalline phases were identified using Jade 2010 v.3 software (Materials Data Inc, Livermore, CA) equipped with the International Centre for Diffraction Data (ICDD) Powder Diffraction File (PDF-4+, 2013).

1.3 - Apatite preparation

Apatite powder was prepared by first combining stoichiometric amounts of CaCO₃ (99.0%, Alfa Aesar), SiO₂ (99.5%, Alpha Aesar) and Y₂O₃ (99.9%, Cerac) or Yb₂O₃ (99.9%, Cerac) powders. The powder mixture was then mixed by ball milling in a HDPE Nalgene bottle with cylindrical zirconia milling media (diameter of 1.27 cm) in acetone for 24 h at 40 RPM. After milling media were separated from the slurry, the slurry was transferred to a glass beaker and heated on a hot plate at ~323 K to facilitate evaporation of the acetone. A mortar and pestle was used to break the resulting powder frit into a powder. The powder mixture was then transferred to a platinum crucible that was heat treated to 973 K at 10 K/min with a 15-minute hold, 1123 K at 2 K/min for 6 h, 1773 K at 10 K/min for 6 hours and then cooled to room temperature at a rate of 10 K/min. The powder frit was removed from the furnace and ground into powder using a mortar and pestle. The powder was heated in a platinum crucible to 1773 K at 10 K/min with a six-hour hold followed by cooling to room temperature at a rate of 10 K/min. The heat treatment procedure was performed one additional time to ensure near full conversion of the powders to apatite, as confirmed by X-ray diffraction and chemical analysis.

1.3.1 - Apatite chemical composition

The chemical composition of the apatite samples measured by inductively coupled plasma optical emission spectroscopy ICP-OES at NSL Analytical Services, Inc., Cleveland, OH.

1.3.2 – Apatite X-ray diffraction

Details of the XRD experiment and data treatment are the same as those given above.

2 – High temperature solution calorimetry

High-temperature calorimetry was performed using a Setaram MHTC-96 calorimeter (Caluire-et-Cuire, France) to determine the enthalpies of drop solution (ΔH_{ds}), solution (ΔH_{s}) and transposed temperature drop (ΔH_{TTD}) of the powder samples. In the HT solution calorimetric experiment illustrated in Fig. 2, sample pellets (~10 mg) of uniaxially pressed coating powder are dropped from room temperature into ~10 g of molten CMAS in a platinum crucible in a Calvet-type calorimeter at 1723 K. The calorimetric experiment measures two heat effects combined, heat content (ΔH_{TTD}) and heat of solution (ΔH_{s}), so that the enthalpy of drop solution $\Delta H_{ds} = \Delta H_{TTD} + \Delta H_{s}$. Measurements were repeated 5–10 times to achieve statistically reliable data. The calorimeter was calibrated against the heat content of corundum. The procedure has been described previously in detail. ³⁵⁻⁴¹

The composition of molten CMAS (30CaO-5.3MgO-11.9Al₂O₃-8.7Fe₂O₃-1.5NiO-42SiO₂ in mole percent, or Ca_{0.3}Mg_{0.053}Al_{0.238}Fe_{0.174}Ni_{0.015}Si_{0.42}O_{1.826}) used for calorimetry was designed by NASA to be similar to that deposited on turboshaft shrouds operated in a desert environment and it is referred here as NASA CMAS.^{1,18} Its calcium to silicon ratio is within the range of the majority of observed siliceous deposits.² This NASA CMAS begins to melt at 1487

K and it is completely molten at ~ 1553 K.¹⁸ The reaction temperature of 1723 K for HT solution calorimetry was chosen to ensure complete dissolution of the samples. The gas temperature within the hot section of jet engines (e.g. combustion chambers and combustor) may reach or exceed this temperature depending on operating conditions.

In the calorimetric experiment a small amount of coating material reacts and dissolves with an effectively infinite amount of molten CMAS. Thus, the discussion of the thermodynamic stability of the coatings in terms of their enthalpies of solution and mixing given below represents a harsh scenario in which CMAS aerosol concentration is high enough to saturate the coatings of the gas-turbines. In this scenario, the gas-turbines operate in dust laden environments such as in a desert environment (e.g. commercial aircrafts flying on Middle East routes, military aircrafts operating in the Persian Gulf) or during volcanic eruption in which millions of tons of ash may be present in the atmosphere. Although the CMAS-to-coating mass ratios of the reactions for apatite formation discussed here are 0.2 to 0.3, they may also represent a harsh CMAS environment if one assumes a high CMAS concentration. Furthermore, even in a scenario with low concentration of aerosol, a gas-turbine is expected to ingest hundreds or thousands of kilograms of CMAS material during its lifetime taking into account the large volume of air during the turbine long operation. Thus, this study is relevant for this scenario as well.

3 – Drop-and-catch calorimetry

3.1 - Sample preparation

Powders of 7YSZ were melted into polycrystalline spheroids \sim 2–2.5 mm in diameter in a copper hearth in air with a 400 W sealed CO₂ laser with 6 mm beam diameter (10.6 mm, Synrad FSi401SB). The copper hearth was placed on the motorized X–Y stage under the beam and the

laser power was adjusted by a LabVIEW controlled laser controller (Synrad UC-2000) which allowed incrementing the power by 0.5%. The high surface tension of rare earth silicate melts produces spheroidal shapes for beads of this diameter.

3.2 – Drop-and-catch calorimetric experiment

The experimental prototype "drop-n-catch" (DnC) calorimeter (Fig. 3) was designed and built in the Peter A. Rock Thermochemistry Laboratory at UC Davis. Detailed description of the laser heating system for operation at temperatures up to 4273 K has been described previously in detail.⁴² Weighed 7YSZ beads were aerodynamically levitated in a splittable nozzle levitator in argon flow, laser heated from ~2973 to 3673 K and dropped into a calorimeter at 298 K, thus measuring enthalpy as a function of temperature. Operating power of the laser was between 0–35%. The levitated solid sample rotates in the nozzle due to surface imperfections and the cavity in the bead formed on quenching from the melt due to volume reduction. The beads continue to rotate by inertia in the molten state for a few seconds. Under such rotation the registered sample temperature is a more accurate representation of the average temperature of the sample.

When the desired temperature was reached, the nozzle was split, dropping the sample into copper catch plates which fully enclosed the sample. Temperature was controlled by manual laser power adjustment through LabVIEW software. The surface temperature (Ts) was measured before each drop with a multiwavelength spectropyrometer (500–1000 nm, 1073–4273 K, 1 s response time, on-line tolerance; FAR Associates).

At the time of the drop, the laser was turned off through LabVIEW software. The delays for splitting the nozzle and catching the sample were controlled and adjusted with LabVIEW software. The total distance of the drop was ~30 mm and it took 104 msec. The heat effects on cooling to 298 K were obtained from integral value of the peak in thermopiles voltage vs. time.

Integration of heat flow during cooling was made in Origin 8.5 software using linear baseline. The fusion enthalpy of 7YSZ was derived from the step in the temperature–enthalpy curve.

4 – Differential thermal analysis (DTA) of ytterbium disilicate and ytterbium apatite

The enthalpy of fusion of ytterbium disilicate and ytterbium apatite samples were measured in a Setaram Setsys Evolution TGA-DTA/DSC differential thermal calorimeter (Caluire-et-Cuire, France) (Fig. 4). Thermal analysis was performed on two Yb₂Si₂O₇ samples and three CaYb₄Si₃O₁₃ samples. These samples were loaded in W crucibles and sealed by TIG welding in Ar flow and heated at 298 K /min to ~2273 K to observe melting endotherm, cooled to ~1673 K to record crystallization peak, then re-heated to ~2273 K to record second melting peak followed by cooling to room temperature. Preliminary analysis was performed with existing calibration of detector using Au melting, and m-t ZrO₂ and HfO₂ transitions. After measurements detector calibration was repeated using Au and Al₂O₃ melting and DTA traces were reanalyzed using new calibration. Calibration uncertainties for 1273-2273 K range are estimated as (±2 K) in temperature and less than 2% in enthalpy (J/g basis).

4.1 – Ytterbium apatite and ytterbium disilicate chemical composition after DTA

After DTA, samples were analyzed by a Tescan MAIA3 TriglavTM scanning electron microscope (Brno – Kohoutovice, Czech Republic) equipped with a X-Max^N energy-dispersive X-ray silicon drift detector (EDS-SSD) (Oxford Instruments, Abingdon, United Kingdom). At least three different grains of each sample were probed by EDS spot analysis.

4.2 – Powder X-ray diffraction (XRD)

The crystalline phases in the samples analyzed by DTA were probed on a Bruker D8 Advance diffractometer (Bruker-AXS, Inc.) using a zero background holder after breaking the

crucibles. The data were acquired from 10° to 90° 20 with a step size of 0.01° using Cu K α radiation.

5 – High temperature X-ray diffraction of yttria stabilized zirconia, and yttrium and ytterbium disilicates mixed with NASA CMAS

The formation of apatite during reaction between a CMAS composition with Yb₂Si₂O₇, Y₂Si₂O₇, and 7YSZ was probed with high temperature X-ray diffraction from room temperature up to 1666 K. Yb₂Si₂O₇ and Y₂Si₂O₇ powders were mixed with CMAS at the stoichiometric amounts assuming apatite formation and the reaction at equilibrium. 7YSZ was mixed with CMAS assuming a 1.0:0.1 molar proportion. 0.048 mol of SiO₂ (Alfa Aesar, 99.5%) was added to the mixture between 7YSZ and CMAS to satisfy the stoichiometry of reaction at equilibrium assuming apatite formation because of the unbalanced amount of calcium and silicon in the CMAS formula Ca_{0.30}Mg_{0.053}Al_{0.238}Fe_{0.174}Ni_{0.015}Si_{0.42}O_{1.826}.

XRD data were gathered on a Panalytical Empyrean diffractometer in Bragg-Brentano (focusing) geometry using Co K α radiation and a Galipix detector in 1D scanning mode. The samples were heated in air using an Anton Paar HTK2000N non-ambient stage with a Pt strip heater. Data was collected after the sample set 5 min on each ~19 min long temperature plateau. Crystalline phases were identified using the same procedure as described above.

Results

1 – Chemical composition and X-ray diffraction of the coatings and apatites

Table 1 gives the details of chemical composition and phase content of the TBC coatings.

The composition of yttrium and ytterbium silicates in terms of oxides is given the Table 2 below.

The heat treated EBC disilicates are single phase, fully crystalline and the chemical composition was confirmed to be the same within the analytical uncertainties as the nominal composition.

The XRD patterns of the yttrium and ytterbium disilicates are presented in Fig. 5. Only monoclinic phases ($P2_1/c$ symmetry, PDF card 04-015-5861 for Y₂Si₂O₇, and C2/m symmetry PDF card 98-001-1269 for Yb₂Si₂O₇) were detected by XRD analysis in the heat treated samples.

,. Chemical composition of the apatites given in Table 3 was confirmed to be the same within the analytical uncertainties as the nominal composition.

The XRD patterns of the yttrium and ytterbium apatites are presented in Fig. 6. Only hexagonal phase ($P6_3/m$ symmetry, PDF card 04-006-0319 for CaY₄Si₃O₁₃, and $P6_3/m$ symmetry PDF card 04-006-0320) was detected by XRD analysis in the apatite samples.

2 - High temperature solution calorimetry

The enthalpies, in units of kJ/g-atom to give a consistent basis of the same number of atoms for comparison, of drop solution, solution and transposed temperature drop of TBCs, EBCs and yttrium and ytterbium apatites are given in Table 4. The average reaction time between the samples and CMAS is also given in Table 1.

3 – Drop-and-catch calorimetry

The enthalpy of fusion of 7YSZ (58 ± 9 kJ/mol or 19.73 ± 3.06 kJ/g-atom) was measured in a custom-made drop-and-catch (DnC) calorimeter. The DnC calorimeter (Fig. 3) measures the enthalpy change when a laser heated aerodynamically levitated sample is dropped into a small calorimeter at room temperature and cooled from temperatures below and above the melting point to ambient temperature. 23 successful drops were performed on five different 7YSZ beads (Table 5).

4 – Differential thermal analysis (DTA) of ytterbium disilicate and ytterbium apatite

The enthalpies of fusion of $Yb_2Si_2O_7$ (151 \pm 8 kJ/mol or 13.73 \pm 0.73 kJ/g-atom) and $CaYb_4Si_3O_{13}$ (240 \pm 11 kJ/mol or 11.43 \pm 0.52 kJ/g-atom) were measured in a Setaram Setsys Evolution TGA-DTA (Setaram, Caluire-et-Cuire, France). The DTA (Fig. 4) obtains calorimetric peaks up to about 2773 K which can be quantified to obtain enthalpies of fusion.

Table 6 summarizes the results of the $Yb_2Si_2O_7$ sample measured by DTA. Melting temperature of $Yb_2Si_2O_7$ was determined as $T_m = 2182 \pm 3$ K with uncertainties as two standard deviation of the mean and number of experiments used for calculations given in Table 6. Both crystallization and melting heat effects were used for calculations of fusion enthalpy. Undercooling in all 4 experiments was less than 10 K. Double peak was observed in some experiments during cooling, although it is not clear wether it is because of an instrumental artefact or due to incongruent crystallization (it is possible that the sample may end up in the upper part of crucible after melting due to wetting of W by silicate melt, although visual examination of broken crucible gives no indication that it has occurred in this case).

Table 7 summarizes the results of the $CaYb_4Si_3O_{13}$ sample measured by DTA. Melting temperature of $CaYb_4Si_3O_{13}$ was determined as $T_m = 2181 \pm 4$ K with uncertainties as two standard deviation of the mean and number of experiments used for calculations given in Table 7. Only melting onset and heat effect on first heating were used for calculations. Samples 2 and 3 exhibited consistent pattern of crystallization enthalpy being half of the fusion enthalpy on first melting. Undercooling on crystallization did not exceed 20 K. Sample 1 which, was longer in molten state temperature than other samples, undercooled more than 200 K on first crystallization and the heat effect on crystallization on second melting was consistent with the heat effect on first melting in samples 2 and 3. Possible interpretation, consistent with observed

heat effects and XRD results of sample 2, is that CaYb₄Si₃O₁₃ was crystallized in Sample 1 at 1910 K. However, crystallization after melting samples 2 and 3 produced Yb₂SiO₅ and glass which partially crystallized to CaYb₄Si₃O₁₃ during cooling. On repeated heating, only melting of Yb₂SiO₅ contributed to DTA peak in these samples which resulted in lower heat effects.

4.1 - Ytterbium apatite and ytterbium disilicate chemical composition after DTA

Chemical analyses were performed on the first set of samples analyzed by DTA (sample 1 in Table 6 and in Table 7). The chemical composition of the ytterbium disilicate sample after DTA (Table 8) is the same within the analytical uncertainty as the as-prepared sample (Table 2). The chemical composition of the ytterbium apatite sample after DTA (Table 8) is the same within the analytical uncertainty as that of the as-prepared sample (Table 3).

4.2 – Powder X-ray diffraction (XRD)

XRD were performed on the second set of samples analyzed by DTA (sample 2 in Table 6 and in Table 7). Only monoclinic phase (C2/m symmetry PDF card 04-007-4857) was detected by XRD analysis in the Yb₂Si₂O₇ sample after DTA, Fig. 7. Ytterbium silicate phase (B2/b symmetry PDF card 01-074-4822, Yb₂SiO₅) was detected by the XRD in the ytterbium apatite sample after DTA besides the initial apatite phase ($P6_3/m$ PDF card 04-006-0320), Fig. 8.

5 – Enthalpy of mixing

The enthalpy of solution can be decomposed into two terms, namely the enthalpy of fusion (ΔH_{fusion}) of the solid phase and the enthalpy of mixing (ΔH_{mix}) between the samples (7YSZ, Yb₂Si₂O₇ and CaYb₄Si₃O₁₃) of supercooled liquid and the CMAS melt. Once the enthalpies of fusion and solution are measured, the enthalpy of mixing is calculated as the enthalpy of solution minus the enthalpy of fusion $(\Delta H_{mix} = \Delta H_s - \Delta H_{fusion})$. The entropy of fusion (ΔS_{fusion}) is

calculated as $\Delta S_{fusion} = \Delta H_{fusion}/T$ where T is the melting temperature of the coating material either obtained from the literature or measured by DTA. For the melting point of the coatings in question, 7YSZ (3001 K) was obtained from the liquidus line at its correspondent composition in the phase diagram of the $ZrO_2-Y_2O_3$ system⁴⁷ and the melting temperature of $Yb_2Si_2O_7$ ($T_m = 2182 \pm 3$ K) and $CaYb_4Si_3O_{13}$ ($T_m = 2181 \pm 4$ K) measured by DTA. The enthalpies of mixing and fusion, and entropy of fusion of 7YSZ, $Yb_2Si_2O_7$ and $CaYb_4Si_3O_{13}$ are given in Table 9.

6 – Enthalpy of reaction assuming apatite formation

We have calculated the enthalpy of reaction assuming apatite formation for TBCs 7YSZ and 31YSZ, and EBCs $Y_2Si_2O_7$ and $Yb_2Si_2O_7$ reacted with molten CMAS. The reactions between the coatings and molten CMAS and their enthalpies are given in Table 10. Although apatite may show a solid solution range $Ca_{2+y}RE_{8+x}(SiO_4)_6O_{2+3x/2+y}$ (RE = rare earth),² we selected $CaY_4Si_3O_{13}$ and $CaYb_4Si_3O_{13}$ compositions for this study since they are similar to those in earlier studies.^{2,21,25} Our calculations and discussion here assume chemical equilibrium conditions and a single CMAS composition, as enthalpies of reaction would be different for other CMAS compositions.

7 – High temperature X-ray diffraction of yttria stabilized zirconia, and yttrium and ytterbium disilicates mixed with NASA CMAS

Fig. 9 shows the XRD patterns of the yttrium disilicate and NASA CMAS powder mixture during heating up to 1666 K. The detected phases at high temperature with their space groups and PDF No are given in Table 11. Yttrium disilicate ($P2_I/c$ symmetry PDF card 04-015-5861) and platinum ($Fm\bar{3}m$ symmetry PDF card 04-001-3300) phases are omitted in Table 11 since their diffraction peaks are present in all temperatures. Besides the yttirum disilicate phase,

the phases detected by XRD with increasing temperature are the following. Mullite and akermanite were detected at 1161 K. Mullite, akermanite and clinoenstatite were detected between 1263 K and 1364 K. Mullite, akermanite and apatite were detected at 1465 K. Apatite was detected between 1566 K and 1666 K. The platinum peak is due to the platinum strip used to support and heat the sample.

Fig. 10 shows the XRD patterns of the ytterbium disilicate and NASA CMAS powder mixture during heating up to 1592 K. The detected phases at high temperature with their space groups and PDF No are given in Table 12. Ytterbium disilicate (C2/m symmetry PDF card 04-007-8967) and platinum ($Fm\bar{3}m$ symmetry PDF card 04-004-6364) phases are omitted in Table S9 since their diffraction peaks are present in all temperatures. Besides the ytterbium disilicate phase, the phases detected by XRD with increasing temperature are the following. Akermanite was detected between 1161 K and 1263 K. Akermanite and enstatite were detected at 1364 K. Akermanite and mayenite were detected at 1465 K. Apatite was detected between 1566 K and 1666 K.

Fig. 11 shows the XRD patterns of the 7YSZ and NASA CMAS powder mixture during heating up to 1666 K. The detected phases at from room to high temperature with their space groups and PDF No are given in Table 13. The phases detected by XRD with increasing temperature are the following. Cubic, tetragonal and monoclinic zirconia and quartz were detected up to 1161 K. Tetragonal and cubic zirconia, walstromite and quartz were detected at 1263 K. Tetragonal and cubic zirconia, and quartz were detected between 1364 K and 1465 K. Tetragonal and cubic zirconia, and zirconium silicate were detected between 1566 K and 1666 K. The phase transformations in 7YSZ are related to dissolution and reprecipitation of material during reaction with CMAS. 18, 24, 48 Zircon detected in this work also has been detected in the

reaction between 7-8 wt % YSZ and volcanic ash at 1250 °C for 5 h. ⁴⁹ The NASA CMAS is mainly amorphous and contains small amounts of akermanite, wollastonite and quartz, and its amorphous phase crystallizes into diopside, akermanite and wollastonite around 1114 - 1229 K. ¹⁸

Other crystalline phases detected in the coatings - CMAS reactions at high temperature may originated from the NASA CMAS during crystallization of its amorphous content or formed during the coatings-CMAS reactions. ¹⁸

Discussion

The reactions between the coatings and molten CMAS are fast, on the order of minutes (Table 4) indicating that they are thermodynamically driven and not kinetically hindered. Given that coatings in service may require over 18,000-24,000 h life durability⁴⁶, these fast rates of reaction can be a major problem since they may result in sudden material failure. Our previous study using conventional furnace tests demonstrated rapid reaction kinetics for air plasma sprayed TBCs reacted with small amounts of CMAS (0.1 CMAS-to-sample mass ratio and CMAS surface concentration (69 to 175 mg/cm²)). 18 Dense EBCs reacted with small amounts of CMAS (9-11 mg/cm², 33CaO-9MgO-6.5A1₂O₃-45SiO₂ in mole %) at 1573 K also exhibited fast kinetics of reaction²³. These earlier studies describing the reaction between TBCs and EBCs with CMAS still did not consider the possibility of continuous ingestion of CMAS during the lifetime of the aircraft engine, which would not only corrode the coatings but corrosion products as well. This includes yttrium and ytterbium apatite phases from EBCs or TBCs. In the present study apatites exhibited fast reaction kinetics (7 - 8 min) with molten CMAS (Table 4). Although the calorimetric measurements carried out on compressed coating powders differ from a turbine environment in which small amount of a CMAS melt is deposited on dense coatings,^{2, 17-34} they still provide important insights into the real problem.

The enthalpies of solution of the coatings and apatites are moderately positive except for the 7YSZ TBC which is slightly negative. The heat of fusion of 7YSZ is endothermic and larger than the observed enthalpy of solution resulting in exothermic enthalpy of mixing (Table 9). Thus the interaction between the two liquids (molten 7YSZ and CMAS) is strongly exothermic and is a driving force for rapid dissolution. The heat of fusion of Yb₂Si₂O₇ and CaYb₄Si₃O₁₃ (Table 9) are similar to their observed enthalpies of solution (Table 4), resulting in slightly exothermic and endothermic enthalpies of mixing (Table 9), respectively. In the case of ytterbium disilicate and apatite, the interaction between the two liquids (molten Yb₂Si₂O₇ or CaYb₄Si₃O₁₃ and CMAS) is not as strong as that between 7YSZ and CMAS, which suggests a higher thermodynamic stability of the former.

Similarly, the entropy of solution is composed of two terms, the entropy of fusion of the solid (which is strongly positive) and the entropy of mixing of the two liquids (which is not known but is also almost certainly positive). Thus the entropy of solution term, being positive, is probably large enough to overcome the small positive enthalpy of solution and give a negative free energy of dissolution for all the materials studied here besides 7YSZ, for which the enthalpy of solution is slightly negative.

At equilibrium, the enthalpy of reaction for apatite formation is given by the difference between the enthalpies of solution of the coatings and apatites (Table 10). Among all the coatings, 7YSZ is the only one for which the enthalpy of the apatite formation reaction is exothermic or energetically favorable ($\Delta H_{reaction} = -4.92$ kJ/g-atom, Table 10). However, this small exothermic term may be overcome by entropic factors which would favor reaction to apatite.

It was observed that the phases that crystallized in the NASA CMAS¹⁸ were different than those that formed between CMAS-coating mixtures. This would suggest that the energetics for apatite formation in the case of the disilicates is favorable when these intermediate phases are present. Since these phases formed in a short time (5 min hold before 19 min data acquisition time) at each temperature plateau during HT XRD, their crystallization is not kinetically inhibited. However they may not represent the equilibrium state of lowest free energy in the system since the stoichiometric amounts used to prepare the CMAS – coatings powder mixtures are based only on the chemical reactions for apatite formation. For the 7YSZ-CMAS reaction, the formation of zircon and quartz in the initial phase assemblage and precipitation of zirconia phases may be more energetically favorable than apatite formation. The thermodynamic cycles discussed here (Table 10) are thus incomplete and the other phases detected by XRD at high temperature could illuminate the thermodynamic pathway of lowest free energy. Other thermodynamic factors that may affect the phase assemblage stability as well are elemental substitutions (Ca can replaced by Mg and Y can be replaced by Al or Fe) in the yttrium disilicate and apatite phases. The kinetic factors which hinder the approach to equilibrium especially at low temperature may include heterogeneity and microstructure of the powder reactants that could affect the ability of the ions to diffuse to form apatite.

The durability and development of gas-turbine ceramic coatings now can be addressed in terms of their thermodynamic stability based on the new calorimetric data. Based on measurements such as those described here, the composition of the coatings may be adjusted to reach higher positive enthalpy of dissolution and subsequently a longer reaction time to form crystalline products and arrest the melt. Alternatively, coatings could be selected for negative enthalpies of formation which would more readily generate reaction products and destabilize the

melt. Our results show that Yb₂Si₂O₇ exhibits higher enthalpic stability (more positive enthalpies of solution and mixing) and longer reaction time during dissolution than 7YSZ, making this material less reactive to CMAS, although it does not provide significant protection from glass infiltration. However, these data suggest that the formation of ytterbium apatite would also be beneficial against CMAS penetration since it exhibits positive enthalpy of mixing with CMAS and therefore could be more stable in contact with the melt once it is formed.

This work demonstrates that the thermodynamic stability of gas-turbine ceramic coatings against molten CMAS reaction can be further explored and used as a guide to create more durable coatings. For example, it might be possible to tailor a coating that, as it dissolves, alters the properties of the melt to inhibit further corrosion by a combination of thermodynamic and kinetic factors. If dissolution produced a melt of greater polymerization degree and higher viscosity, (e.g. a more silica rich composition), dissolution could be slowed or arrested. A more polymerized melt would also potentially diminish the entropy of dissolution. For example, it is well known that the viscosity and crystallization temperature of rare earth containing glasses and melts is affected by the field strength of their rare earths.^{50,51} The viscosity increases and its crystallization temperature increases as the ionic field strength of rare earths increases. The composition of the coating could be engineered to contain specific rare earths such as Gd³⁺, Dy³⁺, Er³⁺, and Sc³⁺ that, once dissolved in molten CMAS, would increase its crystallization temperature and increase its viscosity. Such changes might also make the enthalpy of interaction of the rare earth oxide less favorable. If such a melt were altered to be richer in both silica and the rare earths, it would decrease apatite solubility and favor its crystallization and persistence. One would seek a combination of sacrificial additives to the coating that remained solid at engine operating conditions but then dissolved in the attacking melt particles, making them less

reactive. While all these possible mitigation strategies could provide a solution, thermodynamic stability related to ionic substitution in apatites and rare earth silicates still needs to be experimentally studied in depth. Lower reaction temperatures and other crystalline products described in this study besides apatite also have to be considered in further studies of coating corrosion because of the different temperature (513 - 2073 K) and pressure (60 -140 psia) of operation of gas-turbines. Since the temperatures of crystallization or formation of these corrosion products fall in a wide temperature operation range of gas-turbines, they are as important as apatite formation in mitigating CMAS penetration, thus their thermodynamic properties still need to be experimentally studied in depth.

Conclusions

The enthalpies of reaction between the ceramic coatings (7YSZ, 31YSZ, 16RESZ, Y₂Si₂O₇ and Yb₂Si₂O₇) and apatites (CaY₄Si₃O₁₃ and CaYb₄Si₃O₁₃), and molten CMAS were measured by high temperature solution calorimetry. The enthalpies of mixing between molten CMAS and 7YSZ, Yb₂Si₂O₇ and CaYb₄Si₃O₁₃ were calculated after measuring the enthalpy of fusion of these ceramic coatings and apatite by DnC calorimetry and DTA. The enthalpies of solution of the coatings and apatites are moderately positive expect for 7YSZ. In terms of enthalpy, apatite formation is only favorable over coating dissolution for 7YSZ. Other phases detected by HT XRD in the coating-CMAS reaction are important as apatite formation in thermodynamic pathway of lowest free energy and need to be considered in further studies. The enthalpy of mixing between 7YSZ and molten CMAS is more exothermic than for Yb₂Si₂O₇ and CaYb₄Si₃O₁₃, indicating higher energetic stability of the latter against molten silicate corrosion.

Acknowledgments. This work was supported by the NASA Transformative Aeronautics Concept Program. The calorimetric studies at UC Davis were supported by the Ceramics Program of the Division of Materials Research of the National Science Foundation, Grants DMR 1506229 and 1835848. We are grateful to R. Rogers (NASA Glenn) for assistance with X-ray diffraction and to T. Condrich (NASA Glenn) for the illustration designs.

References

- 1. Borom MP, Johnson CA, Peluso LA. Role of environmental deposits and operating surface temperature in spallation of air plasma sprayed thermal barrier coatings. Surf Coat Technol. 1996;86–87:116–126.
- 2. Poerschke DL, Jackson RW, Levi CG. Silicate deposit degradation of engineered coatings in gas turbines: Progress toward models and materials solutions. Annu Rev Mater Res. 2017;47:16.1–16.34.
- 3. Liu, Z, Hostetler C, Winker D, et al. Airborne dust distributions over the Tibetan Plateau and surrounding areas derived from the first year of CALIPSO lidar observations. Atmos Chem Phys. 2008; 8: 5045–5060.
- 4. Hamed A, Tabakoff W, Wenglarz R. Erosion and deposition in turbomachinery. J Propul Power. 2006; 22: 350 360.
- 5. Campbell E. Recommended flight-crew procedures if volcanic ash is encountered. US Geo. Surv Bull. 1994; 2047: 151-156.
- 6. Krueger BJ, Grassian VH, Cowin, JP, et al. Heterogeneous chemistry of individual mineral dust particles from different dust sources regions: the importance of particle mineralogy, Atmos Environ. 2004; 38: 6253-6261.

- 7. Song WJ, Lavallee Y, Hess KU, et al. Volcanic ash melting under conditions relevant to ash turbine interactions. Nat Commun. 2016; 7: 1-10.
- 8. Padture NP. Advanced structural ceramics in aerospace propulsion. Nat Mater. 2016; 15: 804–809.
- 9. Spitsberg I, Steibel J. Thermal and environmental barrier coatings for SiC/SiC CMCs in aircraft engine applications. Int J Appl Ceram Technol. 2004;1:291–301.
- 10. Padture NP, Gell M, Jordan EH. Thermal barrier coatings for gas-turbine applications. Science 2002; 296: 280–284.
- 11. Evans AG, Clarke DR, Levi CG. The influence of oxides on the performance of advanced gas turbines. J Eur Ceram Soc. 2008; 28: 1405–1419.
- 12. Clarke DR, Oechsner M, Padture NP. Thermal-barrier coatings for more efficient gas-turbine engines. MRS Bull. 2012; 37: 891–898.
- 13. Lee, K. N. Environmental barrier coatings for SiCf/SiC. In: Bansal N P, Lamon J, eds. In Ceramic Materials and Composites: Materials Modeling and Technology. Wiley; 2015; 430-451.
- 14. Lee KN, Fox DS, Eldridge JI, et al. Upper temperature limit of environmental barrier coatings based on mullite and BSAS. J Am Ceram Soc. 2003; 86:1290–1306.
- 15. Lee KN, Fox DS, Bansal NP. Rare earth silicate environmental barrier coatings for SiC/SiC composites and Si3N4 ceramics. J Am Ceram Soc. 2005; 25:1705–1715.
- 16.https://www.safran-aircraft-engines.com/commercial-engines/single-aisle-commercial-jets/leap/leap
- 17. Krause AR, Senturk BS, Garces HF, et al. 2ZrO2·Y2O3 thermal barrier coatings resistant to degradation by molten silicates: Part I, optical basicity considerations and processing. J Am Ceram Soc. 2014; 97: 3943–3949.

- 18. Costa, GCC, Zhu D, Kulis MJ, et al. A. Reactivity between rare-earth oxides based thermal barrier coatings and a silicate melt. J Amer Ceram Soc. 2018; 101: 3674-3693.
- 19. Poerschke DL, Shaw JH., Verma N, et al. Interaction of yttrium disilicate environmental barrier coatings with calcium-magnesium-iron alumino-silicate melts, Acta Mater. 2018; 145: 451–461.
- 20. Stolzenburg F, Johnson MT, Lee KN, et al. The interaction of calcium-magnesium-aluminum-silicate with ytterbium silicate environmental barrier materials. Surf Coat Tech. 2015; 284: 44-50.
- 21. Ahlborg NL, Zhu D. Calcium-magnesium aluminosilicate (CMAS) reactions and degradations mechanisms of advanced environmental barrier coatings. Surf Coat Technol. 2013; 237: 79–87.
- 22. Grant MK, Krämer S, Seward, Gareth GE, et al. Calcium-magnesium alumino-silicate interaction with yttrium monosilicate environmental barrier coatings. J Am Ceram Soc. 2010; 93: 3504-3511.
- 23. Zhao H, Richards BT, Levi CG, et al Molten silicate reactions with plasma sprayed ytterbium silicate coatings. Surf Coat Technol. 2016; 288: 151-162.
- 24. Poerschke DL, Barth TL, Levi CG. Equilibrium relationships between thermal barrier oxides and silicate melts. Acta Mater. 2016; 120: 302–314.
- 25. Darolia R, Nagaraj BA, Konitzer DG, et al. Layered thermal barrier coatings containing lanthanide series oxides for improved resistance to CMAS degradation. U.S. Patent Application US20070160859 A1. 2007.
- 26. Eils NK, Mechnich P, Braue W. Effect of CMAS deposits on MOCVD coatings in the system Y2O3-ZrO2: Phase relationships. J Am Ceram Soc. 2013; 96: 3333–3340.

- 27. Drexler JM, Gledhill AD, Kentaro S, et al. Jet engine coatings for resisting volcanic ash damage. Adv. Mater. 2011; 23: 2419-2424.
- 28. Drexler JM, Chen C-H, Gledhill AD, et al. Plasma sprayed gadolinium zirconate thermal barrier coatings that are resistant to damage by molten Ca-Mg-Al-silicate glass. Surf Coat Technol. 2012; 206: 3911-3916.
- 29. Schulz U, Wolfgang B. Degradation of La₂Zr₂O₇ and other novel EB-PVD thermal barrier coatings by CMAS (CaO-MgO-Al₂O₃-SiO₂). Surf Coat Technol. 2013; 235: 165-173.
- 30. Krämer S, Yang J, Levi CG. Infiltration-inhibiting reaction of gadolinium zirconate thermal barrier coatings with CMAS melts. J Am Ceram Soc. 2008; 91: 576–583.
- 31. Gledhill AD, Reddy KM, Drexler JM, et al. Mitigation of damage from molten fly ash to airplasma-sprayed thermal barrier coatings. Mater Sci Eng A 2011; 528: 7214-7221.
- 32. Turcer, LR, Krause AR, Garces HF, et al. Environmental-barrier coating ceramics for resistance against attack by molten calcia-magnesia-aluminosilicate (CMAS) glass: Part I, $YAlO_3$ and $\gamma-Y_2Si_2O_7$. J Eur Ceram Soc. 2018; 38: 3905-3913.
- 33. Turcer, LR, Krause AR, Garces HF, et al. Environmental-barrier coating ceramics for resistance against attack by molten calcia-magnesia-aluminosilicate (CMAS) glass: Part II, β -Yb₂Si₂O₇ and β -Sc₂Si₂O₇, J Eur Ceram Soc. 2018; 38, 3914-3924.
- 34. Liu J, Zhang L, Liu Q, et al. Calcium-magnesium-aluminosilicate corrosion behaviors of rare-earth disilicates at 1400 °C. J Eur Ceram Soc. 2013; 33: 3419-3428.
- 35. Gan H, Wilding MC, Navrotsky A. Ti⁴⁺ in silicate melts: Energetics from high -temperature calorimetric studies and implications for melt structure. Geochim Cosmochim Acta. 1996; 60: 4123–4131.

- 36. Wilding MC, Navrotsky A. The dissolution of silica and alumina in silicate melts: In situ high temperature calorimetric studies. Neues Jahrbuch f€ur Mineralogie. Rosenhauer Memorial. 1998; 172: 177–201.
- 37. Wilding MC, Navrotsky A. High temperature calorimetric studies of the heat of solution of La₂O₃ in silicate liquids. J Non-Cryst Solids. 2000; 265: 238–251.
- 38. Morishita M, Navrotsky A, Wilding MC. Direct measurement of relative partial molar enthalpy of SiO₂ in SiO₂ M₂O (M=Li, Na, K, Cs) binary and SiO₂ CaO Al₂O₃ ternary melts. J Am Ceram Soc. 2004; 87: 1550–1555.
- 39. Morcos RM, Ellis BG, Navrotsky A. The energetics of hematite dissolution in iron oxide rich melts: In situ high temperature calorimetric studies. Am Miner. 2007; 92: 1064–1070.
- 40. Morcos RM, Navrotsky A. Iron ore sintering: characterization by calorimetry and thermal analysis. J Therm Anal Calorim. 2009; 96: 353–341.
- 41. Koryttseva A, Navorstky A. High-temperature calorimetric study of oxide component dissolution in a CaO-MgO-Al₂O₃-SiO₂ slag at 1450 °C, J Amer Ceram Soc. 2017; 100: 1172-1177.
- 42. Ushakov SV, Shvarev A, Alexeev T, et al. Drop-and-catch (DnC) calorimetry using aerodynamic levitation and laser heating. J Am Ceram Soc. 2017; 100: 754–760.
- 43. Ushakov, SV, Navrotsky A. Experimental approaches to the thermodynamics of ceramics above 1500 °C, J Am Ceram Soc. 2012; 95: 1463–1482.
- 44. Ushakov SV, Navrotsky A. Direct measurement of fusion enthalpy of LaAlO₃ and comparison of energetics of melt, glass, and amorphous thin films, J Am Ceram Soc. 2014; 97: 1589–1594.

- 45. Harris A. Cyclic durability of thermal barrier coatings subject to CMAS attack. *Doctoral Dissertations*. 2018; 1732.
- 46. Halila EE, Lenahan D, Thomas TT. Energy efficient energy: High pressure turbine test hardware detailed design report, NASA-CR-167955, 1982.
- 47. Andrievskaya ER, Kovylyaev VV, Lopato, LM, et al. Powder Metall. Met. Ceram. (Engl. Transl.). 2014; 53: 312-322.
- 48. Stott FH, de Wet DJ, Taylor R. Degradation of thermal-barrier coatings at very high temperatures. MRS Bull. 1994;19:46–49.
- 49. Xia J, Yang L, Wu RT, Zhou YC, Zhang L, Yin BB, Wei YG. On the resistance of rare earth oxide-doped YSZ to high temperature volcanic ash attack.). Surf Coat Technol. 2016; 307: 534-541.
- 50. Shelby JE, Kohli JT. Rare-earth aluminosilicate glasses. J Am Ceram Soc. 1990; 73: 39–42.
- 51. Sasmal N, Garai M, Karmakar B. Influence of Ce, Nd, Sm and Gd oxides on the properties of alkaline-earth borosilicate glass sealant. J Asian Ceram Soc. 2016; 4: 29-38.

Figures and Tables

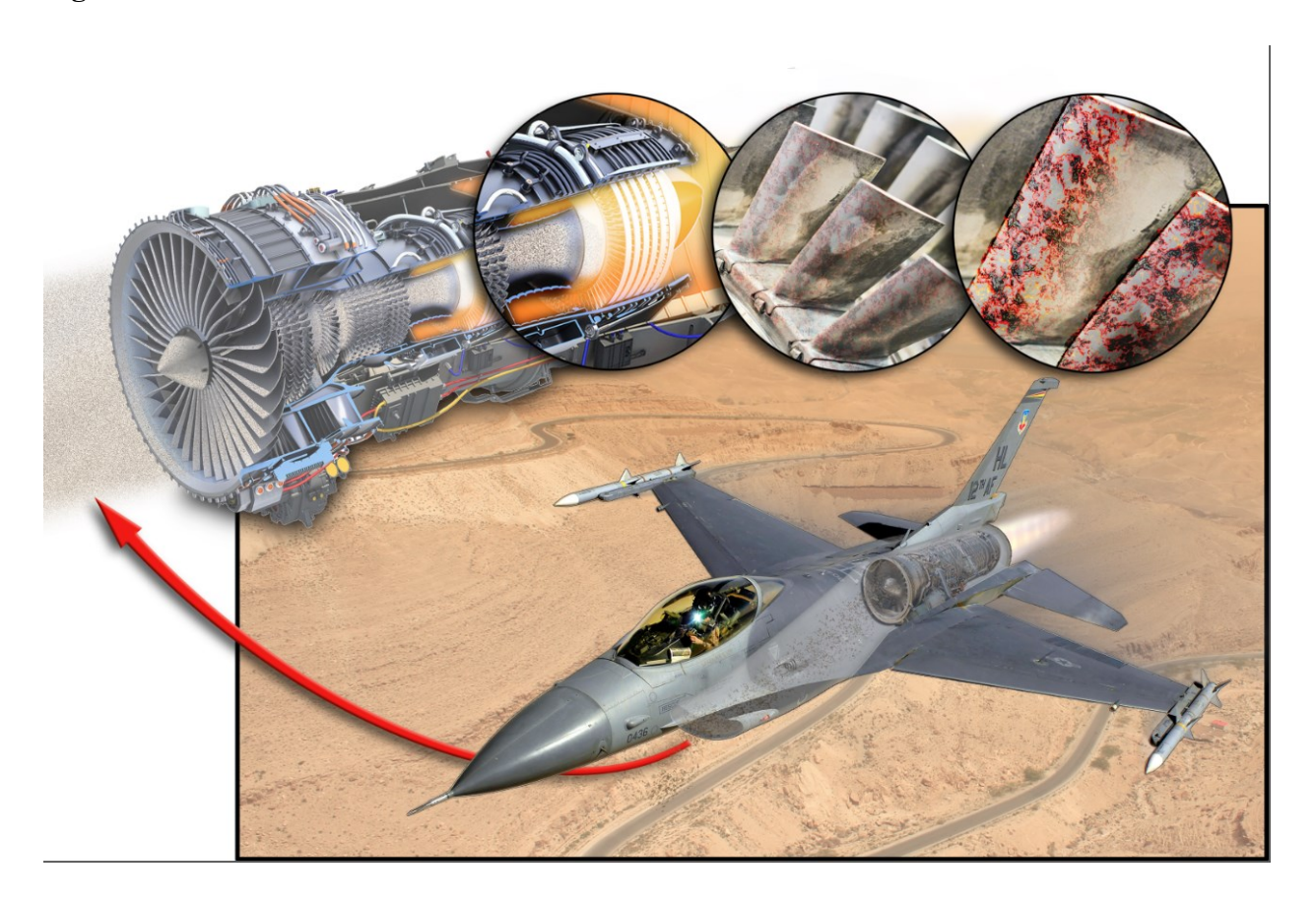


Fig. 1 – Military aircraft flying during a sand storm in an arid region. Image insert – mineral dust particles passing through the gas-turbine and corroding the ceramic coatings and metallic surfaces of the hot section components.

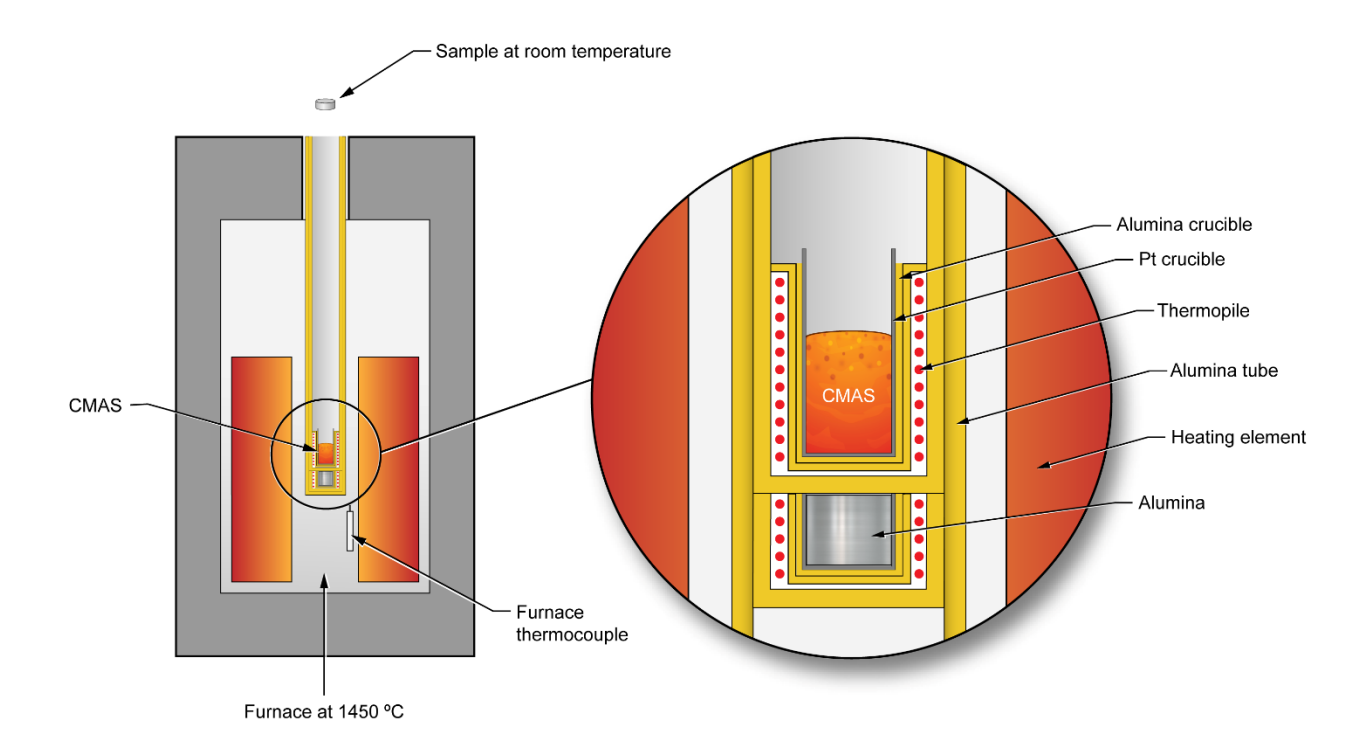


Fig. 2 –High temperature calorimeter and experiment schematic. Sample is dropped from room temperature into Pt crucible with molten CMAS in the calorimeter at 1723 K. Heat involved in the reaction between molten CMAS and samples is measured by thermopile and is converted to enthalpy through a calibration factor.

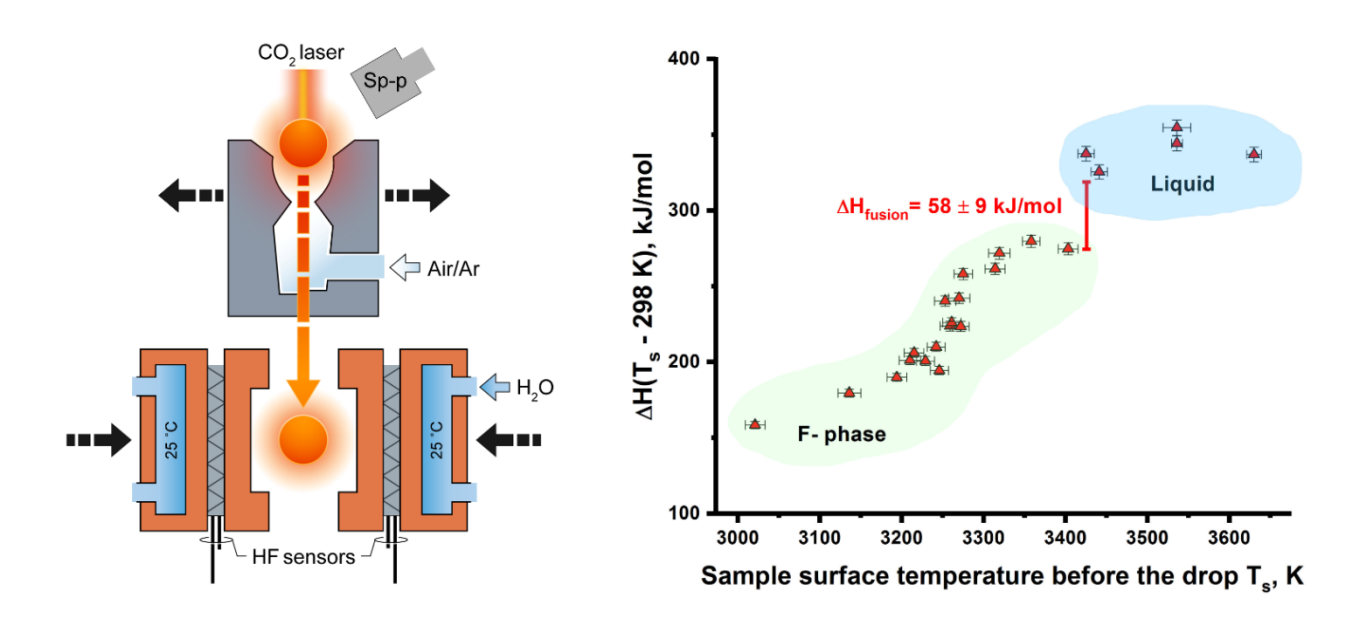


Fig. 3 – Drop-and-catch (DnC) calorimeter schematic (left) and enthalpy versus temperature data from DnC experiments of 7YSZ (right). Aerodynamic levitated sample heated with CO₂ laser is dropped from a splittable nozzle into a calorimeter which catches the sample and measures its heat effect during cooling. Voltage produced at the heat flow sensors is recorded when the calorimeter with sample cools to 298 K.

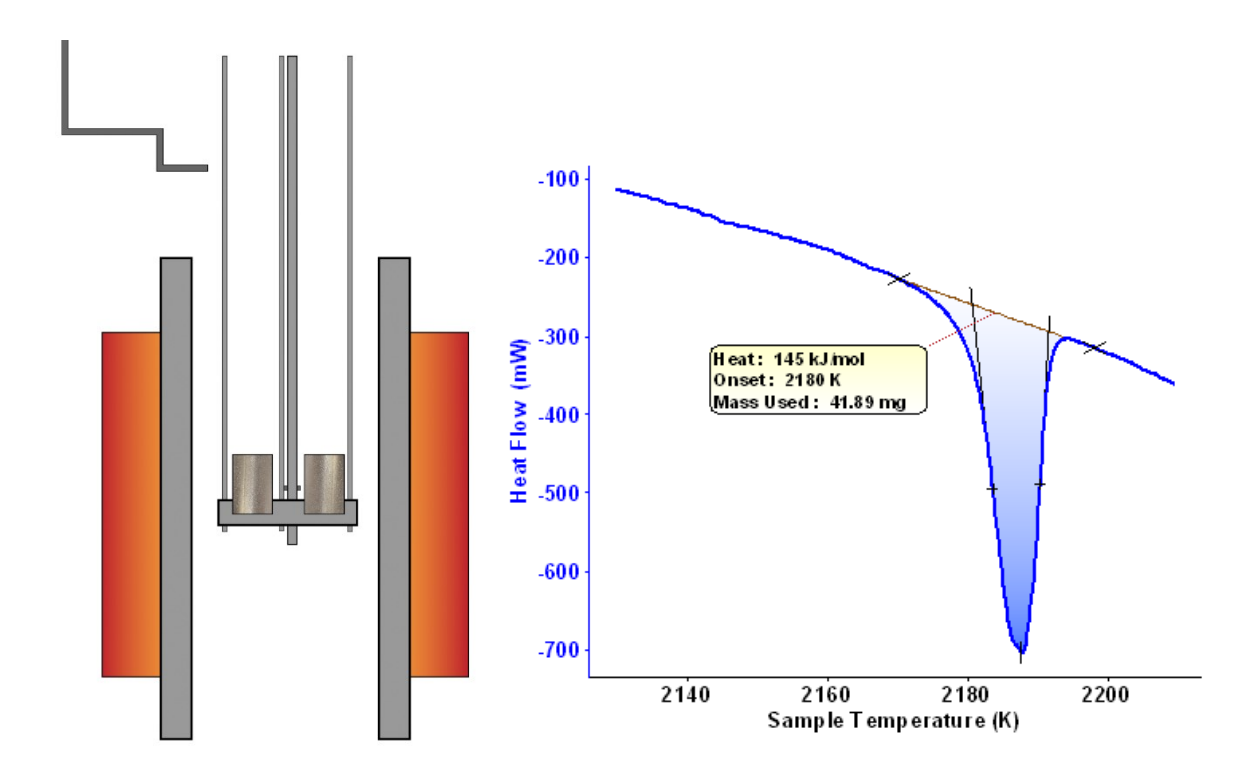


Fig. 4 – Differential thermal analyzer DTA (left) and heat flow versus temperature data from DTA experiment of 1^{st} melting of $Yb_2Si_2O_7$ (right).

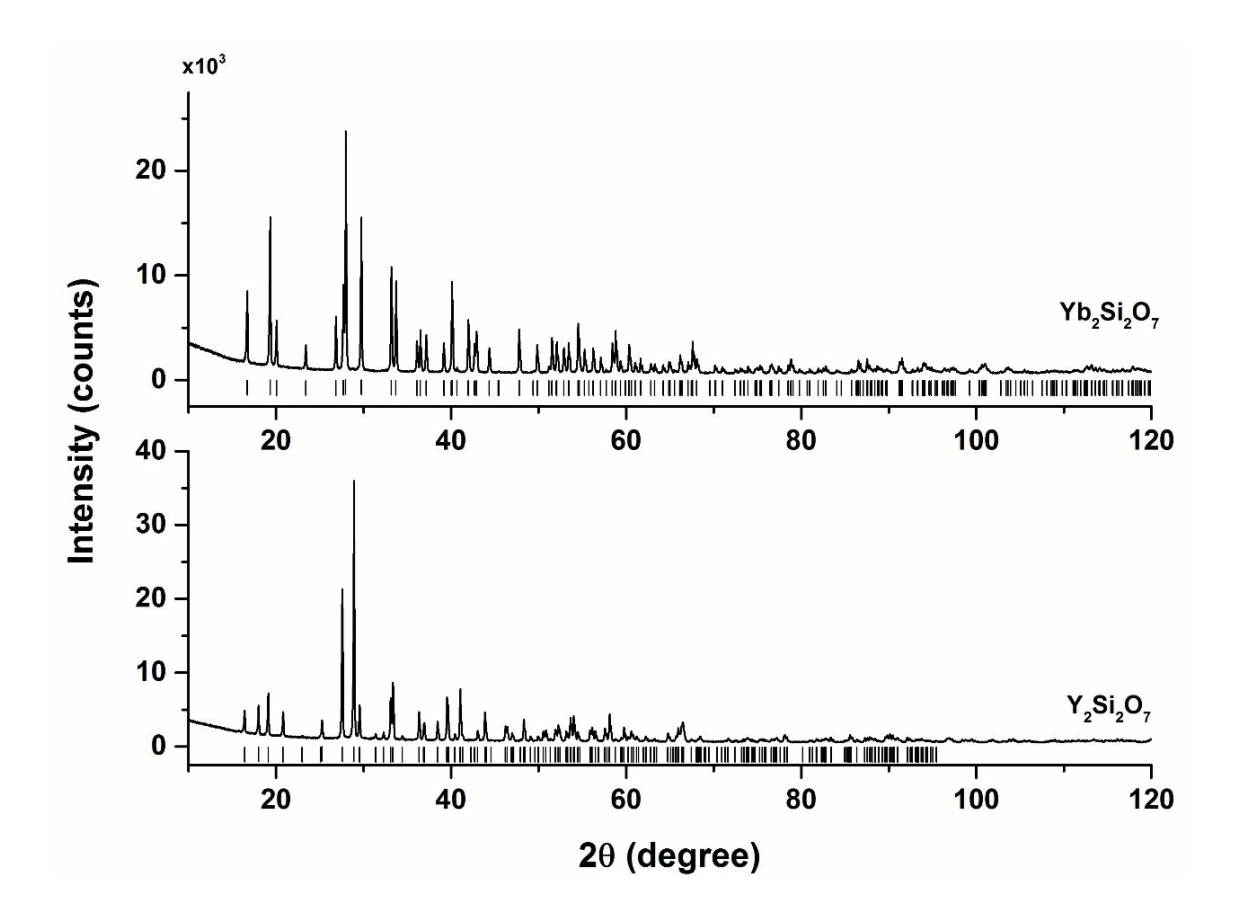


Fig. 5 - X-ray diffraction patterns of yttrium and ytterbium disilicate samples heat treated at 1773 K for 10 h. Tick marks below the patterns show the positions of allowed reflections.

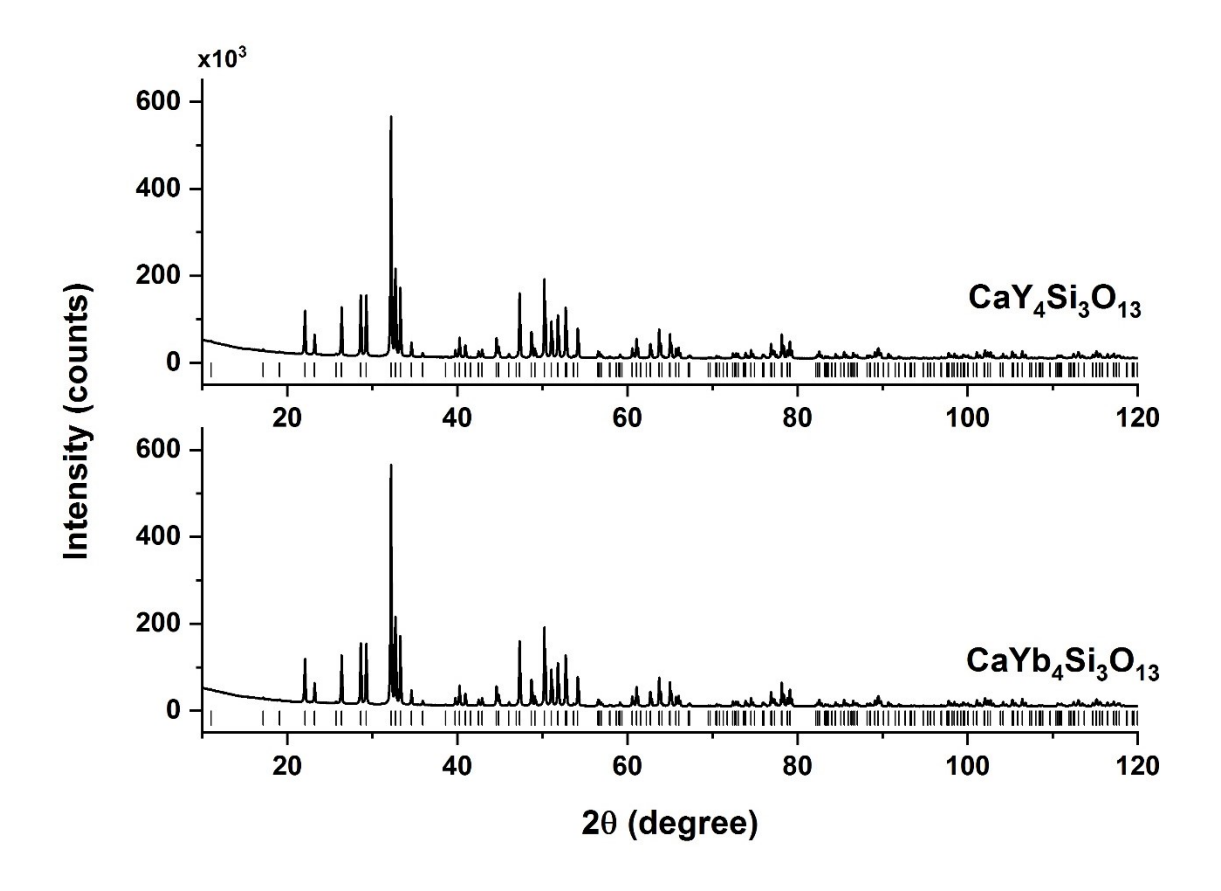


Fig. 6 - X-ray diffraction patterns of yttrium and ytterbium apatite samples.

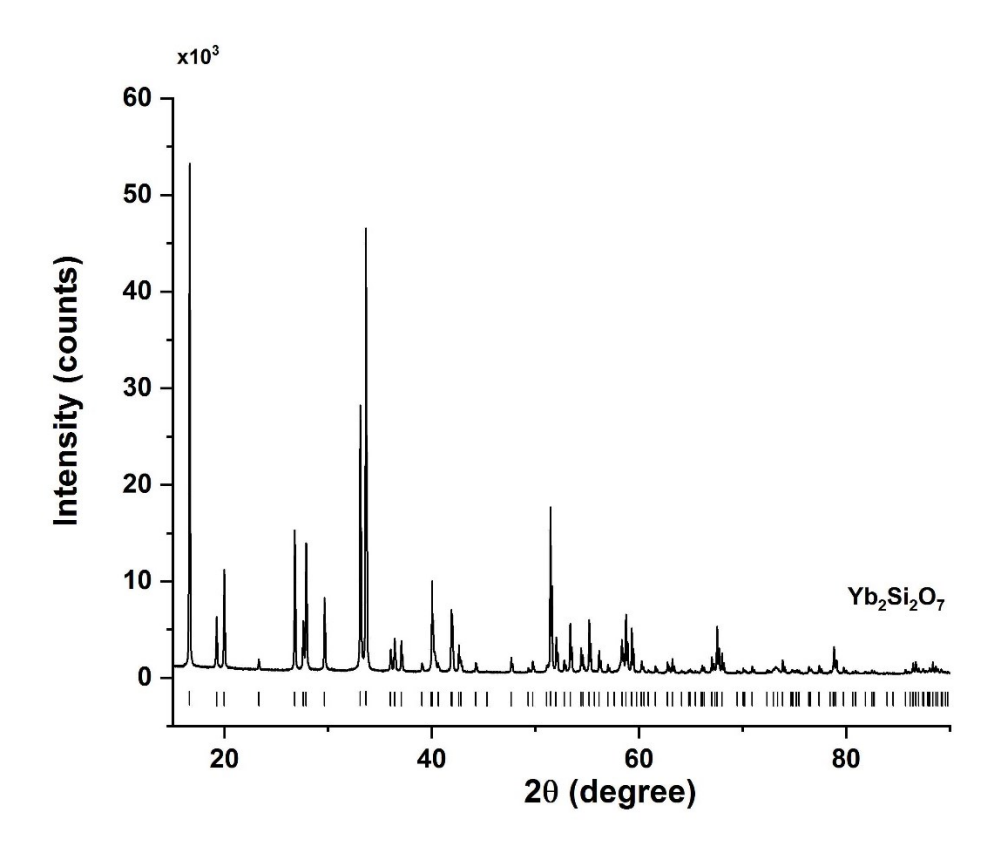


Fig. 7 - X-ray diffraction patterns of the ytterbium disilicate sample after DTA. Tick marks below the patterns show the positions of allowed reflections.

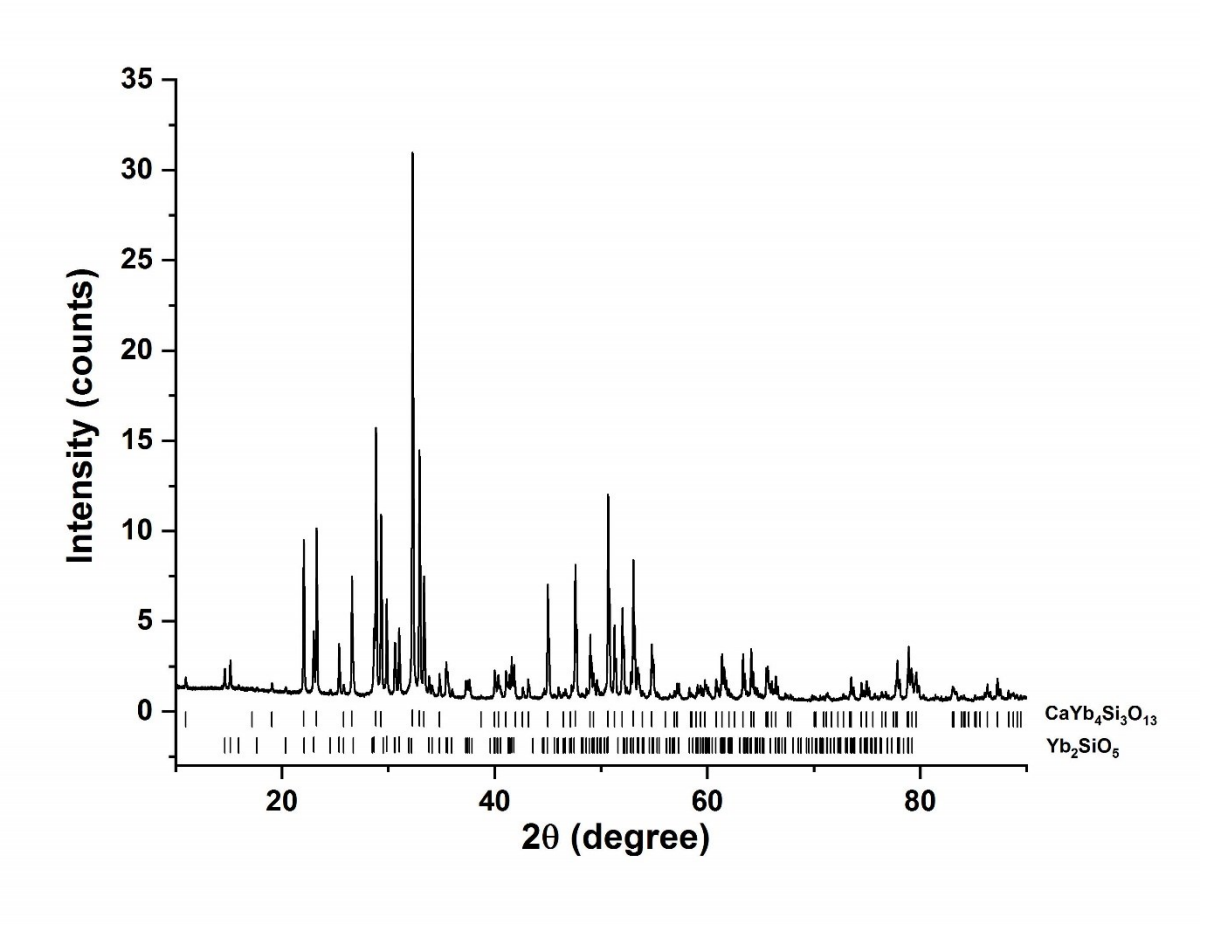


Fig. 8 - X-ray diffraction patterns of the ytterbium apatite sample after DTA. Tick marks below the patterns show the positions of allowed reflections of ytterbium apatite and ytterbium silicate phases.

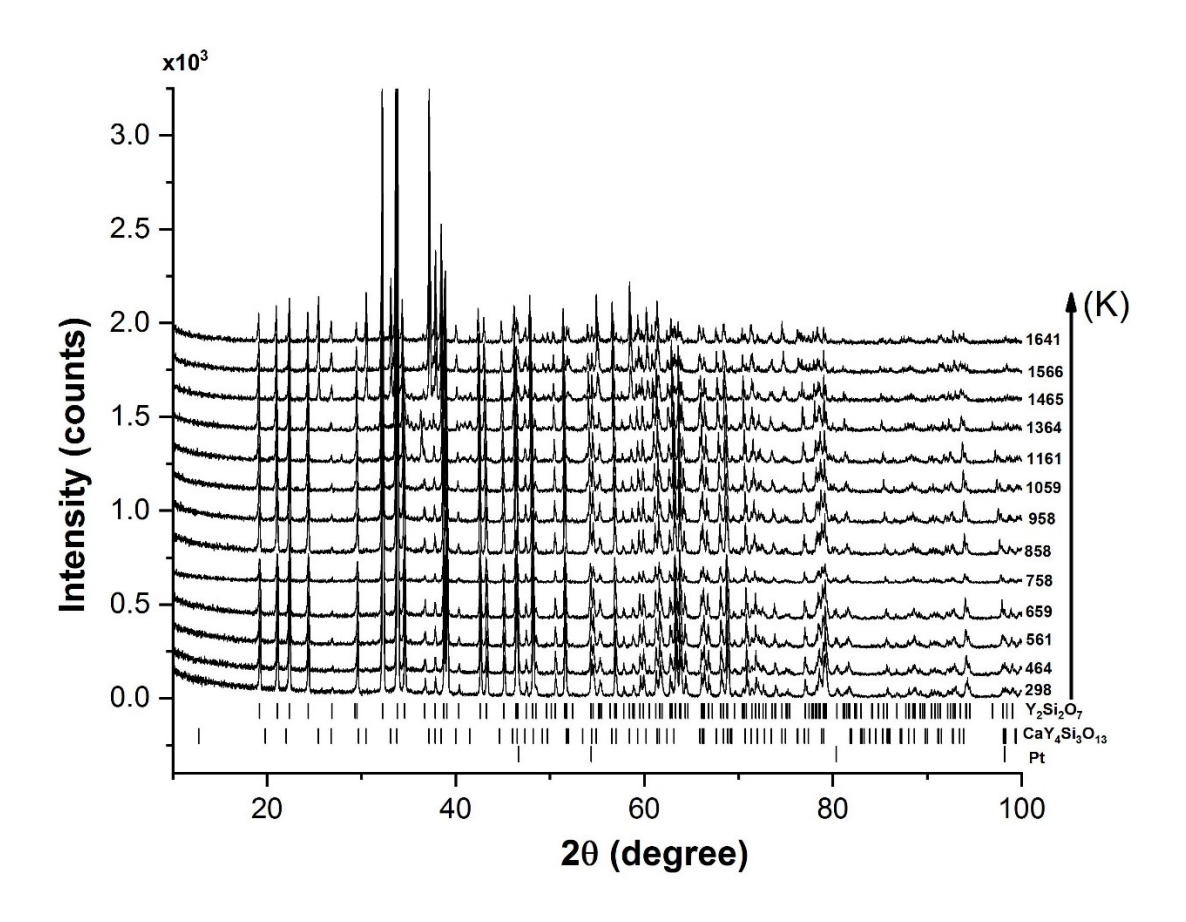


Fig. 9 - X-ray diffraction patterns of yttrium disilicate mixed with NASA CMAS during heating to 1666 K. Tick marks below the patterns show the positions of allowed reflections of yttrium disilicate, akermanite, clinoenstatite, mullite, yttrium apatite and platinum phases.

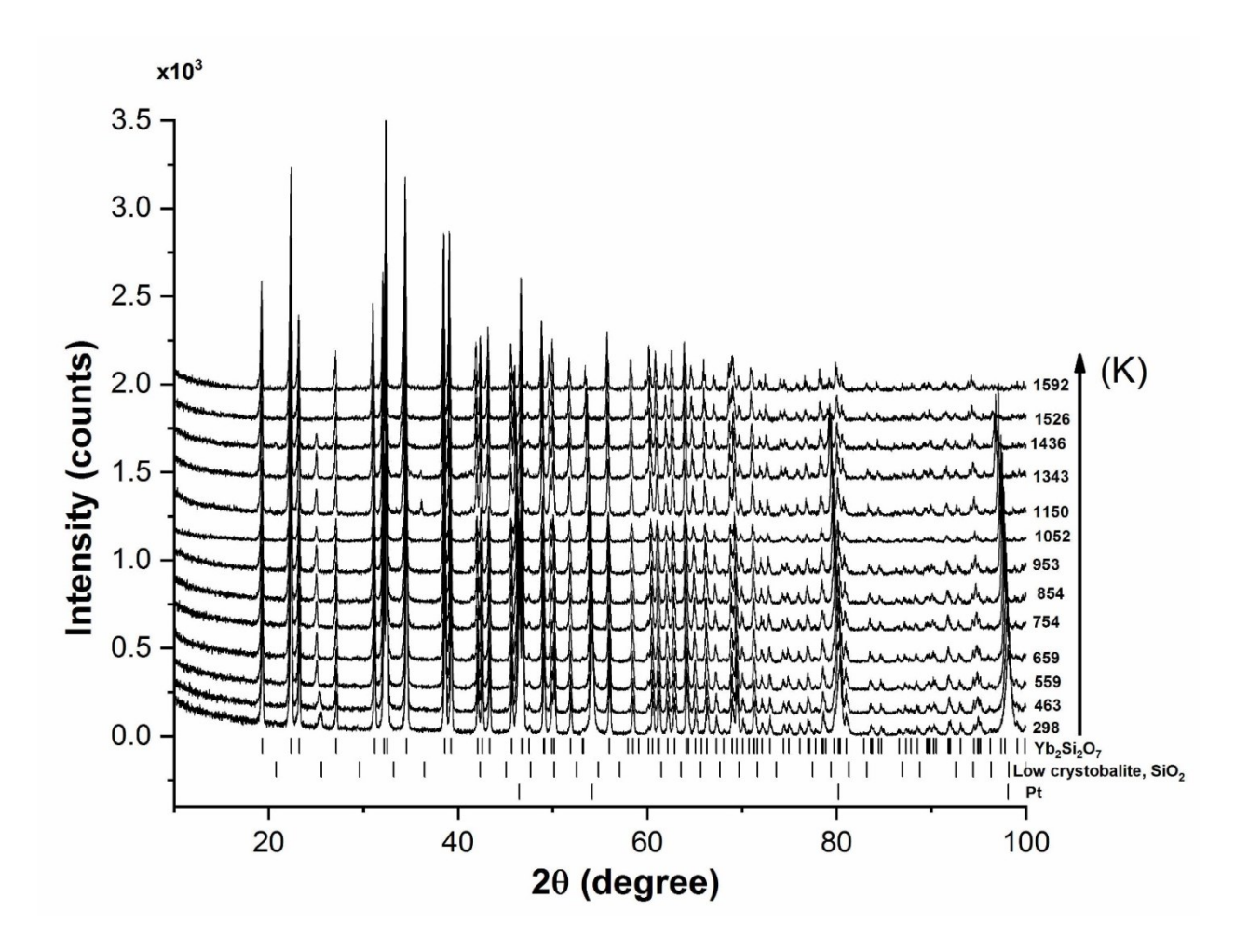


Fig. 10 - X-ray diffraction patterns of ytterbium disilicate mixed NASA CMAS during heating to 1666 K. Tick marks below the patterns show the positions of allowed reflections of ytterbium disilicate, akermanite, enstatite, mayenite, ytterbium apatite and platinum phases.

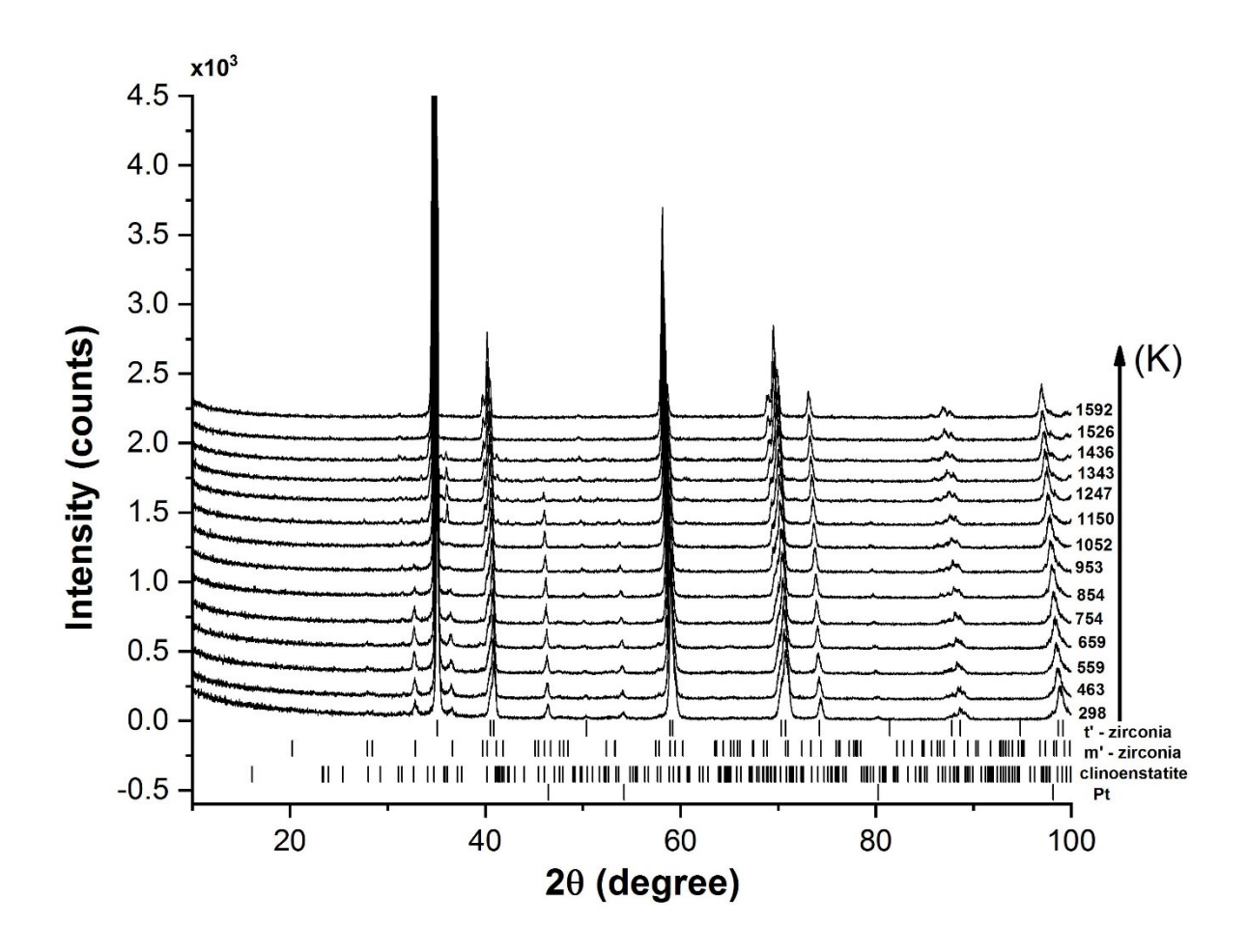


Fig. 11 - X-ray diffraction patterns of 7YSZ mixed with NASA CMAS during heating to 1592 K. Tick marks below the patterns show the positions of allowed reflections of cubic zirconia (c) tetragonal zirconia (t), monoclinic zirconia (m), zirconium silicate, quartz, walstromite and platinum phases.

Table 1 – Phase content and metal oxide content of the zirconia based TBCs.

TPC (nominal composition)	Phase content (wt %)*			Oxide content (mol%)*			
TBC (nominal composition)	Cubic	Tetragonal	Monoclinic	ZrO_2	Y_2O_3	Gd_2O_3	Yb_2O_3
7YSZ	-	97.8(9)	2.2(3)	93(3)	6.6(2)	-	-
31YSZ	100	-	-	69(2)	30.6(9)	-	-
16RESZ	100	-	-	84(3)	10.0(3)	3.3(1)	2.62(8)

^{*}Uncertainties of the contents are given in parentheses.

Table 2 – Metal oxide content of the EBCs.

EDC (nominal composition)	Oxide content (mol%)*			
EBC (nominal composition)	SiO ₂	Y_2O_3	Yb_2O_3	
$Y_2Si_2O_7$	65.3(1)	34.72(5)	-	
$Yb_2Si_2O_7$	66.0(2)	-	34.02(4)	

^{*}Uncertainties of the contents are given in parentheses.

Table 3 – Metal oxide content of the apatites as measured by ICP-OES.

Anatita (naminal aamnagitian)	Oxide content (mol%)*			
Apatite (nominal composition)	CaO	SiO ₂	Y_2O_3	Yb ₂ O ₃
CaY ₄ Si ₃ O ₁₃	15.5(8)	49(2)	36(2)	-
$CaYb_4Si_3O_{13}$	15.3(8)	50(2)	-	35(2)

^{*}Uncertainties of the contents are given in parentheses.

Table 4- Enthalpies of drop solution, transposed temperature drop and dissolution of the coating materials and apatites measured by high temperature calorimetry in molten CMAS at 1723 K.

Material*	Average reaction time (min)	ΔH _{ds} (kJ/mol)	ΔH_{ds} (kJ/g-atom)	ΔH _{TTD} (kJ/mol)	ΔH _{TTD} (kJ/g-atom)	ΔH_s (kJ/mol)	ΔH _s (kJ/g-atom)
7YSZ	7	93.77 ± 1.96	31.86 ± 0.67	107.84 ± 2.72	36.64 ± 0.92	-14.07 ± 3.35	-4.78 ± 1.14
16RESZ	15	143.48 ± 2.88	49.94 ± 1.00	106.96 ± 2.84	37.23 ± 0.99	36.52 ± 4.04	12.71 ± 1.41
31YSZ	20	138.42 ± 1.78	49.97 ± 0.64	88.95 ± 3.77	32.11 ± 1.36	49.47 ± 4.17	17.86 ± 1.51
$Y_2Si_2O_7$	9	540.78 ± 27.83	49.16 ± 2.53	326.74 ± 15.05	29.70 ± 1.37	214.04 ± 31.64	19.46 ± 2.88
$Yb_2Si_2O_7$	11	454.80 ± 5.37	41.35 ± 0.49	318.58 ± 4.69	28.96 ± 0.43	136.22 ± 7.13	12.38 ± 0.65
$CaY_4Si_3O_{13}$	8	640.22 ± 15.52	30.49 ± 0.74	539.74 ± 14.23	25.70 ± 0.68	100.48 ± 21.06	4.78 ± 1.00
$CaYb_4Si_3O_{13}$	7	769.86 ± 7.83	36.66 ± 0.37	526.88 ± 12.90	25.09 ± 0.61	242.98 ± 15.09	11.57 ± 0.72

^{*}Uncertainties are calculated as two standard deviations of the mean. Extra digit is retained to prevent-round off error. Chemical composition of the materials are given in the Supplementary material. 7YSZ ($Zr_{0.88}Y_{0.12}O_{1.94}$), 31YSZ ($Zr_{0.53}Y_{0.47}O_{1.77}$), 16RESZ ($Zr_{0.73}Y_{0.172}Gd_{0.056}Yb_{0.045}O_{1.86}$).

Table 5 – "Drop-and-Catch" experiments on laser heated levitated 7YSZ in argon flow.

#	Sample	Mass	T _s ^a	ΔH (T _s ^a -298 K)
		[mg]	[K]	[kJ/mol]
1		44.78	3021 ± 12	158.5 ± 2.3
2	I	44.76	3136 ± 14	179.6 ± 2.6
3		44.66	3441 ± 10	325.5 ± 4.7
4	II	46.88	3536 ± 7	344.3 ± 4.9
5		50.56	3630 ± 9	337.0 ± 4.8
6		50.54	3194 ± 12	189.9 ± 2.7
7		50.50	3259 ± 12	223.8 ± 3.2
8		50.38	3314 ± 12	261.6 ± 3.8
9		49.94	3425 ± 10	337.5 ± 4.8
10		49.84	3215 ± 12	206.1 ± 3.0
11		49.76	3261 ± 11	226.1 ± 3.2
12	III	49.74	3242 ± 11	210.0 ± 3.0
13		49.70	3210 ± 13	201.2 ± 2.9
14		49.62	3253 ± 13	240.4 ± 3.5
15		49.28	3275 ± 11	258.2 ± 3.7
16		49.21	3270 ± 13	242.2 ± 3.5
17		49.04	3319 ± 13	271.9 ± 3.9
18		48.31	3358 ± 11	279.8 ± 4.0
19		45.71	3229 ± 11	200.7 ± 2.9
20	IV	45.65	3246 ± 11	194.5 ± 2.8
21		45.53	3272 ± 10	223.5 ± 3.2
22		53.29	3403 ± 12	274.7 ± 3.9
23	V	51.32	3536 ± 17	354.7 ± 5.1

^a Surface temperature measured by FAR spectropyrometer

Table 6 - Mass, melting temperature (T_m) , crystallization temperature (T_{xl}) and fusion enthalpy (ΔH_{fusion}) of $Yb_2Si_2O_7$ samples measured by DTA.

Sample	Mass (mg)		$^{\dagger}T_{m}\left(K\right)$	$^{\dagger}T_{xl}\left(K\right)$	$\Delta H_{fusion} \ (J/g)$	ΔH_{fusion} (kJ/mol)
1	41.89	1 st heating	2181		271	139
		1 st cooling		2175	289	149
		2 nd heating	2180		264	136
		2 nd cooling		2173	284	146
2	101.923	1 st heating	2187		330	170
		1 st cooling		2177	324	167
		2 nd heating	2181		291	150
		2 nd cooling		2176	299	154

 $^{^{\}dagger}$ Melting temperature (T_m) is given as onset from melting peak, crystallization temperature (T_{xl}) is given as initial point chosen for integration of peak on crystallization.

Table 7 - Mass, melting temperature (T_m) , crystallization temperature (T_{xl}) and fusion enthalpy (ΔH_{fusion}) of $CaYb_4Si_3O_{13}$ samples measured by DTA.

Sample	Mass (mg)		[†] T _m (K)	[†] T _{xl} (K)	$\Delta H_{fusion} \ (J/g)$	ΔH _{fusion} (kJ/mol)
1	32.32	1 st cooling*		1910	245	251
		2 nd heating	2182		239	245
		2 nd cooling		2161	121	124
2	68.732	1st heating [‡]	2178		229	235
		1 st cooling		2162	118	121
		2 nd heating	2174		107	110
		2 nd cooling**		2113	118	121
3	34.968	1st heating	2184		201	206
		1 st cooling		2169	138	141
		2 nd heating	2179		126	129
		2 nd cooling		2165	141	144

^{*1}st heating was not recorded because of the program crashed; the sample was likely was held longer at 2000 °C, then other samples which may explain much deeper undercooling compare with other experiments. † Melting temperature (T_m) is given as onset from melting peak, crystallization temperature (T_{xl}) is given as initial point chosen for integration of peak on crystallization. **sum of two exothermic peaks.

Table 8 – Metal oxide content of the ytterbium disilicate and ytterbium apatite samples after DTA.

Disilipate/Ametite (maminal assume stition)	Oxide content (mol %)*			
Disilicate/Apatite (nominal composition)	CaO	SiO_2	Yb ₂ O ₃	
$Yb_2Si_2O_7$	-	65.3(9)	34.7(3)	
$CaYb_4Si_3O_{13}$	15.3(2)	50.8(3)	33.9(1)	

^{*}Uncertainties of the contents are given in parentheses.

Table 9 – Enthalpies and entropies of fusion of the coating materials, and enthalpies of mixing between molten CMAS and the coating materials at 1723 K.

Material	ΔH _{fusion} * (kJ/g-atom)	ΔS _{fusion} (J/K/g-atom)	ΔH_{mix} (kJ/g-atom)
7YSZ	19.73 ± 3.06	6.57 ± 1.02	-24.51 ± 3.27
$Yb_2Si_2O_7$	13.73 ± 0.73	6.29 ± 0.33	-1.35 ± 0.98
$CaYb_4Si_3O_{13}$	11.43 ± 0.52	5.24 ± 0.24	0.14 ± 0.89

^{*}The enthalpy of fusion at 1723 K and at the melting temperature of coatings are assumed here to be approximately the same since the effect of differences in heat capacities can be assumed to be small.

Table 10 - Enthalpies of reaction between the coatings and CMAS melt assuming apatite formation.

Reaction						
$ \begin{array}{ll} 1 & Zr_{0.88}Y_{0.12}O_{1.94(xl,1723K)} + 0.09SiO_{2(CMAS,1723K)} + 0.03CaO_{(CMAS,1723K)} = 0.03CaY_4Si_3O_{13(xl,1723K)} + 0.88ZrO_{2(sol,CMAS,1723K)} \\ 2 & Zr_{0.53}Y_{0.47}O_{1.77(xl,1723K)} + 0.3525SiO_{2(CMAS,1723K)} + 0.03CaO_{(CMAS,1723K)} = 0.1175CaY_4Si_3O_{13(xl,1723K)} + 0.53ZrO_{2(sol,CMAS,1723K)} \\ \end{array} $						
$3 Y_2 Si_2 O_{7(xl, 1723 \text{ K})} + 0.5 Ca O_{(CMAS, 1723 \text{ K})} = 0.5 Ca Y_4 Si_3 O_{13(xl, 1723 \text{ K})} + 0.5 Si O_{2(CMAS, 1723 \text{ K})} = 0.5 Ca Y_4 Si_3 O_{13(xl, 1723 \text{ K})} + 0.5 Si O_{2(CMAS, 1723 \text{ K})} = 0.5 Ca Y_4 Si_3 O_{13(xl, 1723 \text{ K})} + 0.5 Si O_{2(CMAS, 1723 \text{ K})} = 0.5 Ca Y_4 Si_3 O_{13(xl, 1723 \text{ K})} + 0.5 Si O_{2(CMAS, 1723 \text{ K})} = 0.5 Ca Y_4 Si_3 O_{13(xl, 1723 \text{ K})} + 0.5 Si O_{2(CMAS, 1723 \text{ K})} = 0.5 Ca Y_4 Si_3 O_{13(xl, 1723 \text{ K})} + 0.5 Si O_{2(CMAS, 1723 \text{ K})} = 0.5 Ca Y_4 Si_3 O_{13(xl, 1723 \text{ K})} + 0.5 Si O_{2(CMAS, 1723 \text{ K})} = 0.5 Ca Y_4 Si_3 O_{13(xl, 1723 \text{ K})} + 0.5 Si O_{2(CMAS, 1723 \text{ K})} = 0.5 Ca Y_4 Si_3 O_{13(xl, 1723 \text{ K})} + 0.5 Si O_{2(CMAS, 1723 \text{ K})} = 0.5 Ca Y_4 Si_3 O_{13(xl, 1723 \text{ K})} + 0.5 Si O_{2(CMAS, 1723 \text{ K})} = 0.5 Ca Y_4 Si_3 O_{13(xl, 1723 \text{ K})} + 0.5 Si O_{2(CMAS, 1723 \text{ K})} = 0.5 Ca Y_4 Si_3 O_{13(xl, 1723 \text{ K})} + 0.5 Ca O_{2(CMAS, 1723 \text{ K})} = 0.5 Ca Y_4 Si_3 O_{13(xl, 1723 \text{ K})} + 0.5 Ca O_{2(CMAS, 1723 \text{ K})} = 0.5 Ca Y_4 Si_3 O_{13(xl, 1723 \text{ K})} + 0.5 Ca O_{2(CMAS, 1723 \text{ K})} = 0.5 Ca O_{2(CMAS, 1723 \text{ K})} + 0.5 Ca O_{2(CMAS, 1723 \text{ K})} = 0.5 Ca O_{2(CMAS, 1723 \text{ K})} + 0.5 Ca O_{2(CMAS, 1723 \text{ K})} = 0.5 Ca O_{2(CMAS, 1723 \text{ K})} + 0.5 Ca O_{2(CMAS, 1723 \text{ K})} = 0.5 Ca O_{2(CMAS, 1723 \text{ K})} + 0.5 Ca O_{2(CMAS, 1723 \text{ K})} = 0.5 Ca O_{2(CMAS, 1723 \text{ K})} + 0.5 Ca O_{2(CMAS, 1723 \text{ K})} = 0.5 Ca O_{2(CMAS, 1723 \text{ K})} + 0.5 Ca O_{2(CMAS, 1723 \text{ K})} = 0.5 Ca O_{2(CMAS, 1723 \text{ K})} + 0.5 Ca O_{2(CMAS, 1723 \text{ K})} + 0.5 Ca O_{2(CMAS, 1723 \text{ K})} = 0.5 Ca O_{2(CMAS, 1723 \text{ K})} + 0.5 Ca O_{2(CMA$	$3 Y_2 Si_2 O_{7(xl, 1723 \text{ K})} + 0.5 Ca O_{(\text{CMAS}, 1723 \text{ K})} = 0.5 Ca Y_4 Si_3 O_{13(xl, 1723 \text{ K})} + 0.5 Si O_{2(\text{CMAS}, 1723 \text{ K})}$					
$4 Yb_2Si_2O_{7(xl, 1723 \text{ K})} + 0.5CaO_{(CMAS, 1723 \text{ K})} = 0.5CaYb_4Si_3O_{13(xl, 1723 \text{ K})} + 0.5SiO_{2(transfer line)}$						
Enthalpy change	ΔH _{reaction} (kJ/mol)	$\Delta H_{reaction}$ (kJ/g-atom)				
$\Delta H_1 = \Delta Hsol \left(Zr_{0.88} Y_{0.12} O_{1.94(xl, 1450^{\circ}C)} \right) - 0.03 \Delta Hsol \left(Ca Y_4 Si_3 O_{13(xl, 1723 K)} \right)$	-17.08 ± 3.58	-4.92± 1.14				
$\Delta H_2 = \Delta Hsol\left(Zr_{0.53}Y_{0.47}O_{1.77(x1,1450 °C)}\right) - 0.1175 \Delta Hsol\left(CaY_4Si_3O_{13(x1,1723 K)}\right) \qquad 37.66 \pm 4.85 \qquad 17.30 \pm 1.51$						
$\Delta H_3 = \Delta Hsol\left(Y_2Si_2O_{7(xl,1450^\circ\text{C})} - 0.5\Delta Hsol(CaY_4Si_3O_{13(xl,1723^\circ\text{K})}\right) \\ 163.80 \pm 33.34 \\ 17.07 \pm 2.92$						
$\Delta H_4 = \Delta Hsol (Yb_2Si_2O_{7(xl, 1450 \circ C)}) - 0.5 \Delta Hsol(CaYb_4Si_3O_{13(xl, 1723 K)})$	14.73 ± 10.38	6.60 ± 0.74				

Table 11 – Crystalline phases detected during heating of $Y_2Si_2O_7$ and NASA CMAS powder mixture up to 1666 K.

Temperature (K)	Phase	Space Group	PDF No
1161	$Al(Al_{1.27}Si_{0.728}O_{4.864})$, mullite	Pbam	01-083-1881
	$Ca_2Mg_{0.75}Al_{0.5}Si_{1.75}O_7$, akermanite	$P\overline{4}2_{I}m$	04-015-7945
1263	$Al(Al_{1.27}Si_{0.728}O_{4.864})$, mullite	Pbam	01-083-1881
	*Ca ₂ Mg(Si ₂ O ₇), akermanite	$P\overline{4}2_{I}m$	04-014-4689
	MgSiO ₃ , clinoenstatite	$P2_{I}/c$	04-016-1671
1364	$Al(Al_{1.27}Si_{0.728}O_{4.864})$, mullite	Pbam	01-083-1881
	**Ca ₂ Mg(Si ₂ O ₇), akermanite	$P\overline{4}2_{I}m$	04-015-7951
	MgSiO ₃ , clinoenstatite	$P2_{I}/c$	04-016-1671
1465	$Al(Al_{1.27}Si_{0.728}O_{4.864})$, mullite	Pbam	01-083-1881
	***Ca ₂ Mg(Si ₂ O ₇), akermanite	$P\bar{4}2_{I}m$	01-087-0046
	Ca ₄ Y ₆ O(SiO ₄) ₆ apatite	$P6_3/m$	00-027-0093
1566	Ca ₄ Y ₆ O(SiO ₄) ₆ apatite	P6 ₃ /m	00-027-0093
1666	Ca ₄ Y ₆ O(SiO ₄) ₆ apatite	P6 ₃ /m	00-027-0093

 $\textbf{Table 12} - \text{Crystalline phases detected during heating of } Yb_2Si_2O_7 \text{ and NASA CMAS powder mixture up to } 1666 \text{ K}.$

Temperature (K)	Phase	Space Group	PDF No
1161	Ca ₂ Mg _{0.46} Al _{1.99} Si _{1.52} O ₇ , akermanite	$P\overline{4}2_{I}m$	98-000-9495
1263	Ca ₂ Mg _{0.46} Al _{1.99} Si _{1.52} O ₇ , akermanite	$P\overline{4}2_{l}m$	98-000-9495
1364	***Ca ₂ Mg(Si ₂ O ₇), akermanite	$P\overline{4}2_{1}m$	01-087-0046
	MgSiO ₃ , enstatite	Pbca	98-000-2666
1465	$Ca_2(Mg_{0.554}Fe_{0.446})Si_2O_{7,a}$ akermanite	$P\overline{4}2_{1}m$	98-001-8297
	$(Ca_{12}Al_{14}O_{32})O_{1.32}$, mayenite	I 4 3d	01-076-7125
1566	CaYb ₄ (SiO ₄) ₃ O, apatite	$P6_3/m$	04-006-0320
1666	Ca ₄ Yb ₆ O(SiO ₄) ₆ apatite	$P6_3/m$	04-006-0320

Table 13 – Crystalline phases detected during heating of 7YSZ and NASA CMAS powder mixture up to 1666 K.

Temperature (K)	Phase	Space Group	PDF No
298-1161	ZrO ₂ cubic	$Fm\overline{3}m$	04-006-5589
	$Zr_{0.868} Y_{0.132} O_{1.934}$, tetragonal	$P4_2/nmc$	04-016-2102
	ZrO ₂ , monoclinic	$P2_{I}/c$	04-013-6875
	SiO ₂ , quartz	P3 ₂ 21	04-015-7194
1263	$Zr_{0.82} Y_{0.16}Al_{0.02}O_{1.91}$, tetragonal	$P4_2/nmc$	04-013-4580
	ZrO ₂ , cubic	$Fm\overline{3}m$	04-006-5589
	CaSiO ₃ , walstromite	$P\overline{1}$	98-001-3613
	α -SiO ₂ , quartz	P3 ₂ 21	04-015-7194
1364	$Zr_{0.82} Y_{0.16}Al_{0.02}O_{1.91}$, tetragonal	P4 ₂ /nmc	04-013-4580
	ZrO ₂ , cubic	$Fm\overline{3}m$	04-006-5589
	α -SiO ₂ , quartz	P3 ₂ 21	04-015-7194
1465	$Zr_{0.82} Y_{0.16}Al_{0.02}O_{1.91}$, tetragonal	P4 ₂ /nmc	04-013-4580
	ZrO ₂ , cubic	$Fm\overline{3}m$	04-006-5589
	α -SiO ₂ , quartz	P3 ₂ 21	04-015-7194
1566	Zr _{0.82} Y _{0.16} Al _{0.02} O _{1.91} , tetragonal	$P4_2/nmc$	04-013-4580
	ZrO ₂ , cubic	$Fm\overline{3}m$	04-006-5589
	Zr(SiO ₄), zircon	$I4_{1}/amd$	04-014-1620
1666	$Y_{0.16}Zr_{0.82}Al_{0.02}O_{1.91}$, tetragonal	$P4_2/nmc$	04-013-4580
	ZrO ₂ , cubic	$Fm\overline{3}m$	04-006-5589
	Zr(SiO ₄), zircon	I4 ₁ /amd	04-014-1620